catalysts

MDPI

Review

The Synthesis and Photocatalytic Efficacy of Distinct Nano-Oxides in the Breakdown of Organic Contaminants

Jelena Pavlović [1], Nataša Novak Tušar [2,3] and Nevenka Rajić [4,*]

[1] Institute of Soil Science, Teodora Drajzera 7, 11000 Belgrade, Serbia; soils.pavlovic@gmail.com
[2] National Institute of Chemistry, Hajdrihova 19, SI-1001 Ljubljana, Slovenia; natasa.novak.tusar@ki.si
[3] Graduate School, University of Nova Gorica, Vipavska 13, SI-5000 Nova Gorica, Slovenia
[4] Faculty of Ecology and Environmental Protection, University "Union, Nikola Tesla", Cara Dušana 62–64, 11158 Belgrade, Serbia
* Correspondence: nrajic@unionnikolatesla.edu.rs

Abstract: Nano metal oxides (NMOs), with their unique physico-chemical properties and low toxicity, have become a focus of research in heterogeneous catalysis. Their distinct characteristics, which can be tailored based on size and structure, make them highly efficient catalysts. NMOs have the potential to significantly contribute to the degradation of numerous environmental pollutants through photolytic decomposition. This work comprehensively analyzes the synthesis, catalytic performance, and applications of photocatalytically active metal oxides, specifically titanium, zinc, copper, iron, silver, tin, and tungsten oxides. The primary objective is to demonstrate how the effectiveness of photocatalytic processes can be enhanced and optimized by incorporating metals, non-metals, and metalloids into their structure and forming heterostructures. Furthermore, the aim is to understand the underlying process of photocatalytic oxidation thoroughly. Photocatalysis, a promising approach in advanced oxidation processes, has garnered significant interest in these fields.

Keywords: nano oxides; photocatalysis; advanced oxidation processes; synthesis; organic pollutants

Citation: Pavlović, J.; Tušar, N.N.; Rajić, N. The Synthesis and Photocatalytic Efficacy of Distinct Nano-Oxides in the Breakdown of Organic Contaminants. *Catalysts* **2024**, *14*, 771. https://doi.org/10.3390/catal14110771

Academic Editor: Jorge Bedia

Received: 26 September 2024
Revised: 25 October 2024
Accepted: 25 October 2024
Published: 31 October 2024

1. Introduction

Nanoparticles (NPs) exhibit distinct physical and chemical properties due to their large surface area relative to their volume and the impact of their small size at the quantum level. NPs have diverse applications in electronics, catalysis, energy storage, environmental remediation, biology, and other fields [1,2]. Nano metal oxides (NMOs) exhibit exceptional catalytic activity, specific adsorption properties, high electrical conductivity, and magnetic traits. They are frequently utilized as catalysts in chemical reactions or as sensors in electronic systems [3–5]. Extensive research into NMOs is leading to innovative methods for their production [6], new methodologies for their characterization, and uncovering new uses for these adaptable NPs. With the ongoing progress of technology, NMOs will probably have a growing significance in influencing the future of many areas.

Advanced oxidation processes (AOPs) are chemical treatment methods for eliminating organic and inorganic contaminants from water and wastewater. This is achieved by generating hydroxyl radicals (•OH), which possess strong reactivity and can effectively degrade complex pollutants such as organic dyes, pesticides, or pharmaceuticals [7–10]. AOPs are highly efficient in breaking down diverse organic contaminants resistant to removal through traditional treatment methods.

Photolytic advanced oxidation processes (PAOPs) employ ultraviolet (UV) radiation to produce •OH through the oxidation of molecules like hydrogen peroxide (H_2O_2) or ozone (O_3). Hydroxyl radicals are generated by activating photocatalysts, such as the widely used titanium dioxide (TiO_2), by UV radiation and initiating the generation of electron–hole pairs in the photocatalyst, which react with water and oxygen, creating •OH.

Due to their unique features and high efficiency, semiconductor NMOs have been extensively studied and utilized in photocatalysis. In Figure 1, band gap positions of different semiconductors in contact with an aqueous electrolyte are shown.

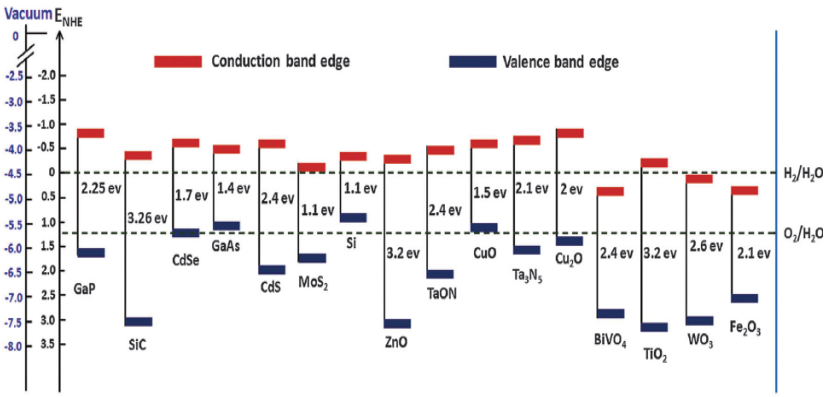

Figure 1. A comparative view of band edge locations of several semiconductors in contact with an aqueous electrolyte (pH = 0) is conducted on the conventional hydrogen electrode, the vacuum level, and the redox potentials of water splitting [11].

The most frequently employed semiconductor NMOs in photocatalysis are titanium dioxide (TiO_2), zinc oxide (ZnO), and iron oxide (Fe_2O_3). Several more candidates show promise for utilization in photocatalysis. They exhibit photocatalytic behavior upon exposure to light, typically in the ultraviolet (UV) spectrum, as they generate electron–hole pairs upon photon absorption. On the catalyst's surface, the energized electrons and vacancies can participate in oxidation–reduction reactions, leading to the decomposition of organic pollutants, the splitting of water into hydrogen, or other specific chemical transformations. NMOs have several advantages in photocatalysis, such as a large surface area to volume ratio, customizable band gap energy, chemical stability, and cost-effectiveness. Recently, various approaches have been explored to enhance the light to energy conversion efficiency of NMOs. These include modifying their surface properties, incorporating additional elements, and fabricating nanostructures to optimize light absorption and charge separation. In general, NMOs exhibit significant promise for applications in environmental remediation, energy conversion, and other disciplines that require efficient and sustainable photocatalytic processes. It should be noted that using suspended photocatalysts for wastewater treatment is common, but it presents numerous drawbacks, such as photocatalyst saturation or the necessity for recovery and post-treatment following photocatalytic procedures, which are expensive and challenging to execute. One approach is to immobilize photocatalysts on supports to address these issues. Using NMO photocatalysts in the membrane diminishes fouling and improves its effectiveness. Improving membrane applications by incorporating photocatalysts and membrane technology is linked to the enhanced hydrophilicity and antibacterial properties of photocatalysts. The decreased contact angle of the treated membrane indicates the hydrophilic properties of the composite membrane. The composite membrane's anti-fouling characteristics promote the development of a hydrophilic thin layer via hydrogen bonding, thus preventing the attachment of fouling materials to the membrane surface [12].

The use of NMO NPs in photocatalysis has attracted considerable attention recently, leading to increased published literature, including review papers. A bibliometric analysis has demonstrated the evolution of the importance of this research topic in the literature over the last decade [13]. This increase is due to the necessity for developing water purification solutions in response to rising global environmental degradation. Review articles concentrate on specific components, such as contaminants, particular metal oxide particles, or innovative materials like BiOBr nanocomposites. Srinisava performed a comprehensive review highlighting current progress in applying diverse photocatalysts to remove emerging pharmaceutical contaminants in wastewater [14]. Krishnan et al.

conducted a study of current research trends in transition metal oxide-based photocatalysis for the elimination of organic dyes from water [15]. The review included synthesizing BiOBr-based nanocomposites, the mechanisms that boost photocatalytic activity, and their present research state, and possible applications in destroying organic pollutants was also published [16].

This paper thoroughly examines synthetic methods and the catalytic efficacy and uses of photocatalytically active metal oxides, namely titanium, zinc, copper, iron, silver, tin, and tungsten oxides. The main goal is to show how the efficacy of photocatalytic processes can be improved and maximized by integrating metals, non-metals, and metalloids into their framework, forming heterostructures. Importance is also given to the methods of synthesis of metal oxide particles, with particular emphasis on the advantages and disadvantages of individual methods.

2. Synthesis

2.1. Wet Chemical Methods

2.1.1. Sol–Gel Methods

Due to its compatibility with industrial use, the sol–gel method is a widely studied wet chemical technique for manufacturing NMOs. One of its benefits is the ability to manage the size and uniformity of NMOs effectively. Nevertheless, this method is constrained by an organic solvent, which can bring environmental risks, restricted availability, costly starting materials, and a protracted reaction duration.

Usually, metal alkoxide, the molecular precursor, is dissolved in water or alcohol and converted to gel by heating and stirring by hydrolysis/alcoholysis. Producing a homogenous sol from the molecular precursor and its subsequent transformation into a gel is the most crucial step in the sol–gel process. Most often, the citrate sol–gel approach is used. Citric acid is a chelating agent that bonds metal cations and lowers reaction temperatures [17]. The citric acid sol–gel method effectively synthesizes nano mesoporous La_2O_3 [18]. The procedure applies to synthesizing binary, ternary, and quaternary metal oxides in crystalline and amorphous forms. The essential advantage of this method, as with the more traditional sol–gel process, is the homogeneity of the starting material.

The sol–gel technique provides numerous benefits for the creation of NMOs. It allows for manipulating the size and shape of nanoparticles, producing uniform and consistent particles [19]. By using proper solvents and pH in the synthesis of TiO_2, a high photocatalytic efficiency was achieved by band gap engineering [20]. However, it is essential to note that the sol–gel method may not be appropriate for synthesizing specific types of nanoparticles or materials [21]. Furthermore, this method has several drawbacks. The technique can be laborious and require several sequential stages [22].

2.1.2. Hydrothermal Method

The hydrothermal process occurs at high pressures and temperatures above the boiling point in water-based solutions. NMOs usually form in solution from metal precursors at 80–200 °C. This method allows for tuning the morphology of NPs, improving specific properties for specific applications. It has been traditionally used to create different types of ZnO nanoparticles, such as nanorods and nanowires [23]. Hexagon-shaped nano SnO_2 was successfully prepared by a simple hydrothermal route [24], as well as Ga_2O_3 nano cuboids [25], NiO in the form of nano petals [26], nano-MnO [27], and nano-V_4O_9 plates [28]. The main disadvantages of this approach are the synthesis at high pressure and temperatures, the complicated experimental setup, and, most importantly, the limited potential for scale-up manufacturing.

2.1.3. Coprecipitation

This is an economically efficient and uncomplicated technique that enables the large-scale manufacturing of NMOs. The process entails manipulating variables such as temperature, pH, solvent selection, and precipitating agent to customize the characteristics of

the nanoparticles. The process is effective for the synthesis of ZnO and CuO. However, it may lead to the formation of clumps, necessitating adjustments. CuO nanoparticles with a high purity level and a crystalline structure were synthesized using $CuCl_2$ and NaOH as precursors and CH_3COOH as a capping agent. The particle size was narrowly from 21.88 nm to 22.14 nm [29]. The synthesis of nano-ZnO powder was achieved via oxalate coprecipitation methodology. Zinc oxalate dehydrate was converted into zinc oxalate on calcination at 500 °C and into ZnO at 700 °C [30].

The cocurrent coprecipitation method was developed as an enhanced version of the traditional coprecipitation method. This method involves the simultaneous addition of a metal salt solution and a precipitant while maintaining the constant pH value of the reaction system. The approach ensures the simultaneous precipitation of multiple cations. Nano-powder ZrO_2, garnet, and perovskite were obtained by cocurrent coprecipitation [31]. Recently, the method was applied to synthesize complex nano-sized Dy_2O_3–Sc_2O_3 co-stabilized ZrO_2 powders [32].

The hypergravity coprecipitation technique is used in the industrial production of nano calcium carbonate, nano iron oxide, and nano cerium dioxide powder. This technique uses a hypergravity rotating bed to create a chemical reaction between two liquid phases, resulting in minor films, filaments, and droplets. This process enhances micro-mass transfer and separation between the metal salt solution and precipitant, forming a protective layer on the particles. The hypergravity method addresses uneven particle size, inadequate powder dispersion, and particle clumping, making it suitable for industrial manufacturing [33].

Chemical precipitation is a cost-effective and scalable method for producing NMOs with controlled structures and morphologies. It effectively synthesizes ZnO and CuO nanoparticles but may cause agglomeration issues, requiring modifications.

2.1.4. Electrochemical Methods

The increasing interest in electrochemical synthesis for preparing NMOs is motivated by its simplicity, low-temperature operation, low energy consumption, greater product purity, and ecological friendliness. Recent advancements in this method have shown the ability to manipulate the composition and morphology of these structures without the need for adsorbing capping agents [34]. Electrochemical deposition (cathodic and anodic), cathodic corrosion, and galvanic exchange reactions are usually applied [35]. Applying a pulsed potential waveform during Cu_2O electrodeposition in alkaline electrolytes enables the formation of Cu_2O films with a controllable morphology without altering the electrolyte composition or temperature [36]. Cathodic corrosion produces NMOs and mixed NMOs with an excellent particle size and shape homogeneity, significantly improving photocatalyst nanoparticle synthesis procedures. Amorphous TiO_2 and crystalline H_2WO_4 and $BiVO_4$ nanoparticles were prepared (Figure 2) with a preferential crystallographic orientation starting from the base metal as the reactant [34]. This method is ripe for industrial scale-up, as it avoids large volumes of organic solvents and significant investments in heating, cleaning, safety, and disposal issues.

Nanotubular TiO_2, possessing an average inner pore width of roughly 110 nm, was synthesized in a meticulously regulated process using electrochemical anodization in an aqueous phosphoric acid solution, including hydrofluoric acid [37]. The anodization cell voltage affects the pore diameter of TiO_2 nanotubes, with a voltage of 20 V yielding the biggest pore diameter and the maximum conversion efficiency under light. Moreover, hydrofluoric acid has a substantial role in pore formation and dissolution. The produced materials were assessed as photoanodes for dye-sensitized solar cells utilizing metal phthalocyanine dyes.

Galvanic replacement reaction also yields metal nanostructures with controlled shapes, morphologies, and compositions [38]. In this process, one metal (often known as a sacrificial template) is oxidized by the ions of another metal having a higher reduction potential. The template undergoes oxidation and dissolution by coming into touch with a solution. Simultaneously, the ions of the second metal undergo reduction and are deposited onto

the external surface of the template. Galvanic replacement reactions provide a simple and versatile route for producing hollow nanostructures with controllable pore structures. Nanocrystals of Mn_3O_4 react with $Fe(ClO_4)_2$, forming hollow box-shaped nanocrystals of Mn_3O_4/γ-Fe_2O_3 ("nanoboxes"), which are ultimately transformed into hollow cage-like nanocrystals of γ-Fe_2O_3 ("nanocages") [39]. It is important to note that this approach can only be used for a limited number of highly reactive metal oxides. Using somewhat raised temperatures is necessary due to the relatively sluggish kinetics, which might be considered a disadvantage compared to standard electrochemical approaches.

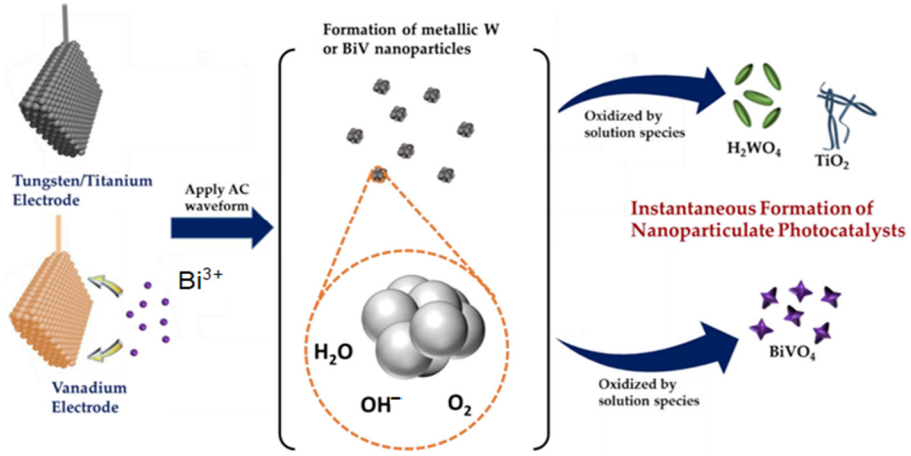

Figure 2. Schematic illustration of the cathodic corrosion processes for preparing H_2WO_4, TiO_2, and $BiVO_4$ [34].

2.1.5. Chemical Vapor Deposition

Chemical vapor deposition (CVD) is a flexible method for creating NMOs, offering benefits like homogeneity, scalability, and control over flakes. However, it has drawbacks like cost and hazardous gas safety issues. Recently, a graphene coating on nano-TiO_2 was applied using CVD, resulting in a composite material with superior photocatalytic activity and anti-fouling properties. Graphene improved pollutant adsorption and increased the TiO_2's charge separation and transportation, resulting in a positive anti-fouling effect [40]. A highly active photocatalyst based on Fe-doped nano-sized TiO_2 was successfully synthesized by chemical vapor deposition (CVD) using $FeCl_3$ as an iron source [41]. The growth of Mo-doped ZnO thin films on glass substrates was achieved by aerosol-assisted CVD, operating at ambient pressure [42]. Mo is present in the 4+ oxidation state, contributing two electrons to electrical conduction for every Zn^{2+} ion replaced in the lattice. SnO_2 nanowires and nanoribbons (doped and pure) have been synthesized using the CVD method and Sn and SnO_2 powders as precursors [43].

2.1.6. Spray Pyrolysis

This method of the production of NMO powder involves consistently blending chemical components in solution to obtain a complex solution, which is then sprayed into a high-temperature reaction furnace (Figure 3). An ultra-fine MO powder is created in the furnace through an instantaneous spray pyrolysis reaction. The following are some of this method's benefits: (1) the whole process can be made relatively simple by eliminating steps like the mixing, calcining, and milling of solid powder; and (2) mixing with impurities can be minimized, and the various pyrolysis reaction conditions can adjust the characteristics of the produced particles. Many manufacturers—including Merck, Scimarec, and the American company SSC—create beneficial ceramic powders by spray pyrolysis [44]. The method produced nano-NiO powder using $NiCl_2$ solution as a raw material. The concentration of the solution and atmospheric pressure influence the powder's properties. The average particle size at 700 °C is about 20 nm, increasing by temperature [44]. Similarly, spray pyrolysis can prepare nano-CoO powder with an average particle size below 50 nm from

$CoCl_2$. The authors reported that as the reaction temperature increases, the crystallinity gradually increases, yet the specific surface area gradually decreases [45].

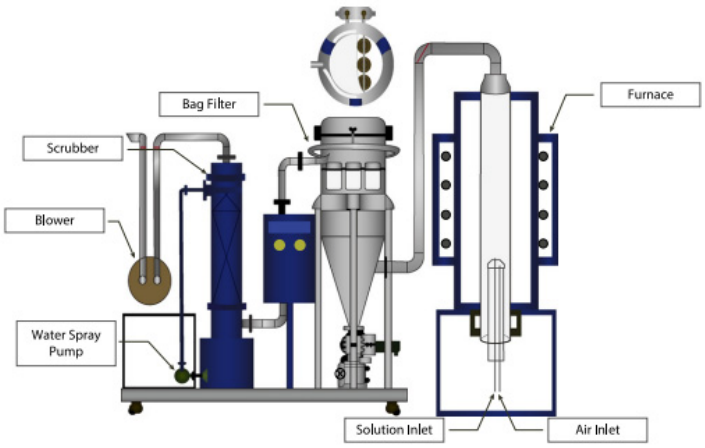

Figure 3. Schematic diagram of a spray pyrolysis system [45].

Although spray pyrolysis is a versatile, simple technique, it has certain limitations, such as requiring the precise control of deposition parameters, the complex reaction mechanism that disables the prediction of the final product, and several environmental concerns due to solvent emissions. Moreover, equipment, solvents, and energy consumption costs can be significant, especially for large-scale production.

2.1.7. Microwave Method

Microwave-assisted synthesis (MW) is frequently used to synthesize NPs, ensuring a uniform heat distribution. This results in regulated physicochemical properties and a restricted size distribution. Recent developments in MW synthesis have mainly been due to the introduction of high-tech microwave reactors, leading to rapid advancements in nanomaterial synthesis [46]. The technique helps produce ZnO-NPs in various sizes and morphologies. This hydrothermal technique has been successfully used to manufacture flower-type, needle-type, and spherical-type NPs [47]. By MW heating for 20 min at 180 °C, fine anatase TiO_2-NPs with a crystal size of around 7 nm and a specific surface area of 220 $m^2\ g^{-1}$ can be produced [48]. A high level of photocatalytic activity has been reported. Furthermore, the crystallization of nano-CeO_2 photocatalysts doped with F and Fe is possible by an MW–hydrothermal treatment, which enhances photoelectric characteristics, electron and hole separation, and visible light catalytic activity due to homogeneous crystal structures and large specific surface areas [49].

The MW technique was recently used to prepare heterostructures like ZnSe/ZnO (Figure 4), which have a high visible area adsorption efficiency [50]. A facile one-pot MW-assisted synthesis also obtained metal-free In_2S_3/In_2O_3 nanosheets (Figure 5) [51] effective in photocatalytic water splitting under blue LED light irradiation.

While MW-assisted synthesis is a valuable technique for producing nanomaterials, it also has disadvantages, including the necessity for real-time reaction monitoring in MW reactors, which makes reaction parameter optimization difficult, and scaling up for commercial production.

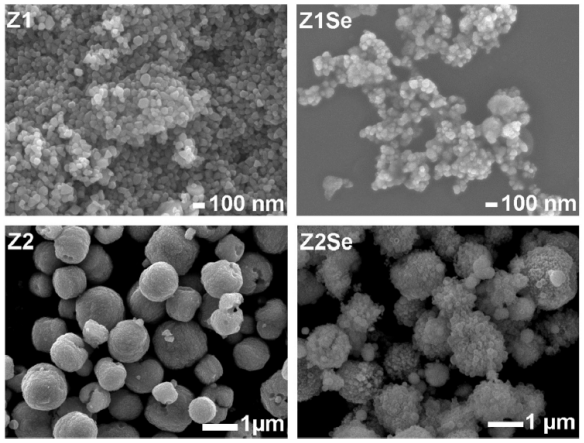

Figure 4. SEM images of ZnO heterostructures Z1 and Z2, synthesized with the microwave-assisted hydrothermal method with zinc acetate and zinc nitrate as a source of Zn^{2+} ions, respectively, along with the corresponding Se-containing ZnO heterostructures on Z1 and Z2 [50].

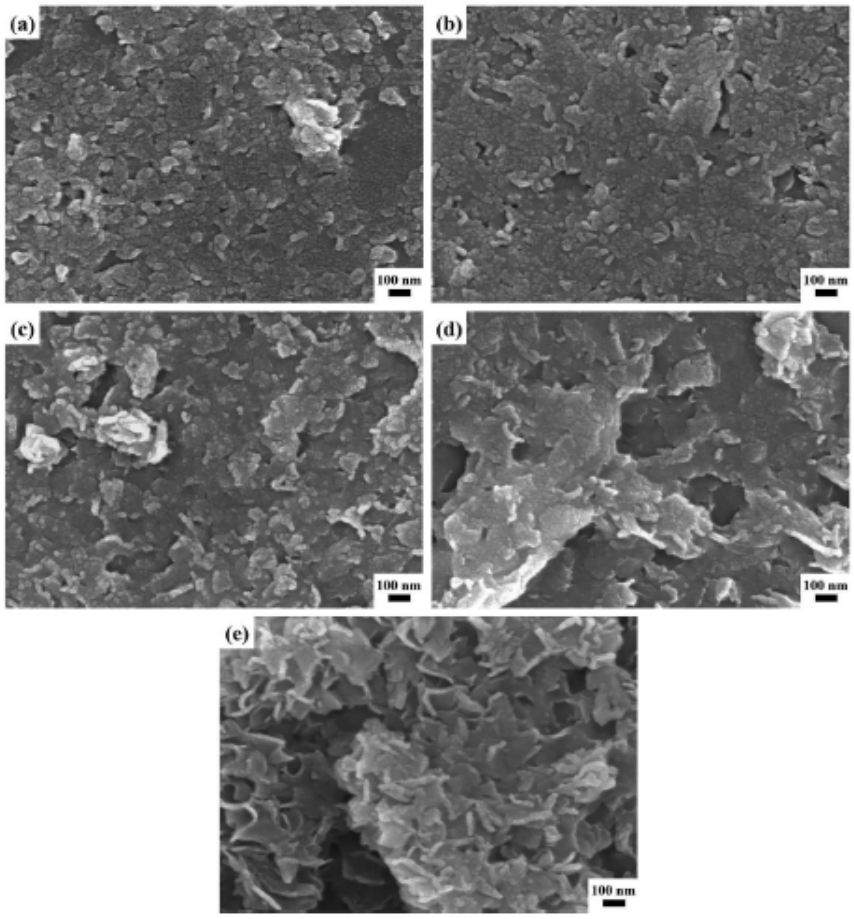

Figure 5. FESEM images of In_2S_3/In_2O_3 nanosheets synthesized at different concentrations of $InCl_3$ at 150 °C for 30 min. The concentrations of $InCl_3$ are (**a**) 2.5, (**b**) 5, (**c**) 10, (**d**) 20, and (**e**) 30 mM, respectively [51].

2.2. Solid-Phase Synthesis

Solid-phase synthesis obviates the need for a liquid medium to produce NPs generated from solid precursors, addressing a significant constraint of liquid-phase synthesis. This solution-phase approach allows for the dependable and reproducible synthesis of nanomaterials with precise dimensions and configurations. However, the extensive use of

solvents, capping agents, and additional separation procedures required for this method leads to the generation of dangerous waste. It limits the scalability of the synthesis due to its high costs.

Solid-phase synthesis has garnered attention due to its potential to produce NPs with distinct features. The process often entails mechanical milling and solid-state processes conducted in a controlled environment, such as an inert gas, to avoid oxidation or contamination. Cooperative coprecipitation in the solid state can occur when precursor solids are combined and heated to enhance reactivity, crystallization, and sol–gel processes using solid precursors.

Notable disadvantages include restricted particle size and form control, high energy demands, challenges in NPs aggregation, and a lengthy synthesis duration. However, although solid-phase synthesis has several disadvantages, it is nonetheless a valuable, easy, and cost-effective method for synthesizing NPs. This is especially true when combined with other techniques or tailored for specific purposes.

Solid-state synthesis yielded a visible light-driven photocatalytic system verified for model methylene blue decomposition based on ZnO nanoparticles, natural clay, and TiO_2 nanoparticles [52]. The synthesis included mechanically grinding the components and calcinating the mixture at 700 °C. $Ni(OH)_2$-TiO_2 nanocomposites (with a particle size of about 50 nm) with an acceptable degree of dispersion were designed and successfully synthesized by facile, simple, and eco-friendly solid-state synthesis at room temperature [53].

2.3. Green Methods

Green synthesis processes use plant extrication, plant parts, bacteria, yeast, fungi, and algae to create nanostructures [54]. These methods are cost-effective, pollution-free, and easier to process than traditional methods. The green approach reduces environmental damage and allows for the development of impurity-free nanomaterials. The synthesis of ZnO-NPs using natural materials, such as microbes and plant parts, is advantageous due to their phytochemical constituents acting as capping and reducing agents. Natural materials reduce zinc to the zero-valance state, adding oxide through calcination. Moreover, zinc ions in natural extract solutions form complexes with phytochemicals, and then through hydrolysis, ZnO-NPs are formed. Thus, ZnO nanoparticles were effectively manufactured via a green, straightforward, and environmentally acceptable method, wherein ethanolic extract of *O. europaea* fruit waste served as a capping and reducing agent [55].

Microbes are another biological approach for preparing ZnO-NPs. However, this technique has certain limitations in contrast to plant extract synthesis. It is essential to screen the microbes, which is a time-consuming procedure [56]. Figure 6 shows a schematic presentation of the green procedure for designing NPs from plant extract.

An excellent review of the biosynthesis of ZnO-NPs, its challenges, and potential solutions has recently been reported [56].

The green synthesis of TiO_2-NPs has been performed using several plant extracts (*Cicer arietinum* L. extract, Aloe Vera leaf extract, Annona squamosa fruit peel, and Acanthophyllum laxiusculum). These plants contain a rich source of metabolites, making them suitable for the rapid synthesis of NPs [57].

Bacterial extracts were employed to synthesize green TiO_2-NPs. Bacterial metabolites, similar to plant extracts, significantly impact the decrease and stability of TiO_2. *Lactobacillus* sp. and *Saccharomyces cerevisiae* mediated the biosynthesis of TiO_2-NPs with an NP size of 8–35 nm. A biosynthesis mechanism influenced by pH and redox potential is proposed [58].

A recent study utilized bitter olive seeds and a sol–gel approach to make a nanocomposite of $ZnO-TiO_2$ doped with iron ions [59]. The nano photocatalyst demonstrated high efficacy in treating industrial wastewater samples, with a dye degradation efficiency of over 75%. The device underwent successful semi-industrial testing, demonstrating its effectiveness under UV and visible light.

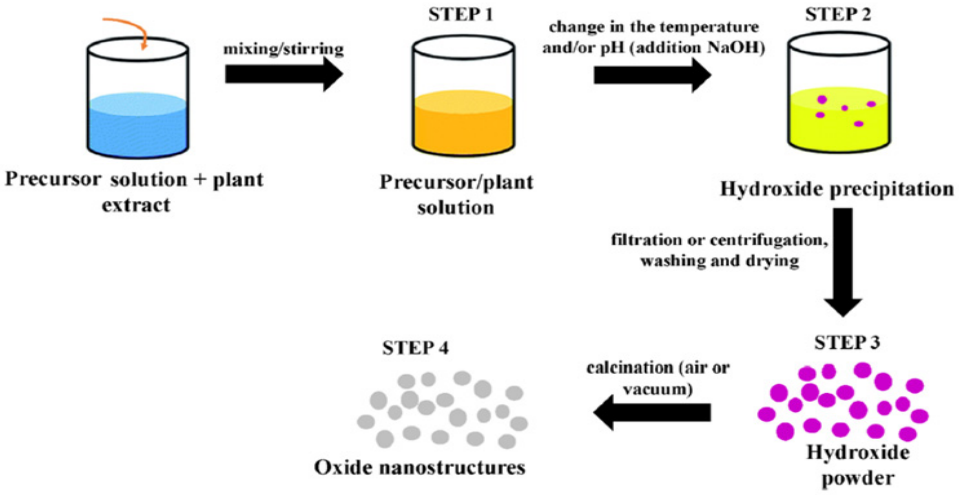

Figure 6. Schematic presentation of the sequential process of green synthesis for creating nanostructures from plant extract [56].

3. Most Common Methods for Enhancement of Photocatalytic Properties

3.1. Doping

Doping is the most frequently used approach for enhancing NMO electrical, optical, and structural properties and altering their electrical, catalytic, optical, structural, and magnetic properties to meet specific needs. It can be performed with metals and non-metals.

Many studies are based on doping the host lattice with rare earth element ions, primarily due to their exceptional conductivity, magnetism, electrical characteristics, electrochemical behavior, and luminescence. Among the many rare earth elements, ions like Sm, Nd, La, Pr, Ce, Gd, etc., have the unique characteristic of having a half-filled shell with 7f electrons, setting them apart from other elements. Rare earth elements exhibit high conductivity due to incompletely filled 4f highly localized orbitals and are insulated by the $5s^2$ and $5p^6$ orbitals in the outer shell. Jimkeli Singh and Chinnamuthu utilized the combustion approach to produce Ce-doped CuO nanoparticles [60]. They found that with an increased cerium concentration, crystallite size and band gap decreased. Ce dopants did not affect the peak positions but reduced intensity. Ce (4 mol.%)-doped CuO NPs showed the highest efficiency in the photocatalytic degradation of rhodamine and methylene blue under solar irradiation [60].

TiO_2's limited absorption in the visible range is a challenge to overcome. Its wide band gap absorbs only UV light, making photocatalysts for the whole solar spectrum exciting. Doping TiO_2 with transition metals, such as Fe, Sb, or Cr, can improve its response under visible light, enhancing photocatalytic efficiency [61]. Plasmonic composites combining TiO_2 with highly dispersed Au nanoparticles can generate OH• radicals under visible light illumination [62].

Non-metal doping offers advantages over metal doping, such as modifying photocatalytic NMOs without thermal instability or poor solubility. Incorporating nitrogen, carbon, sulfur, fluorine, or iodine, possibly as quantum dots [63], is a more efficient way to lower the band gap of TiO_2 and increase photoactivity [63]. The red shift of the S-doped TiO_2 absorption edge was explained with additional extrinsic electronic levels introduced by sulfur doping. This extends the absorption edge to the visible light region [63].

One innovative application is developing nanocomposites with TiO_2 and reduced graphene oxide doped with nitrogen, which shows excellent results in CO_2 photoreduction [64]. The enhancement of TiO_2-based composite with a low carbon-based component ratio for improved hydrogen generation via photocatalytic water splitting was reported [65]. Nitrogen-doped mesoporous TiO_2 (TiO_2-N) is a highly advanced photocatalyst with promising applications, showing a boosted visible light absorption due to shifting 2p orbital levels [66].

Recently, a trimetallic Cu-Mn-Fe silica-supported catalyst was prepared via direct synthesis by incorporating magnetic Fe_3O_4 nanoparticles and active catalytic/photocatalytic species (Cu and Mn) during the formation of the silica nanoparticles with interparticle mesoporosity. In the silica support, the Fenton-like activities of the catalyst result from the catalytic disproportionation of H_2O_2 by Cu^{2+} species and separated Mn species. The catalyst showed a high efficiency in the homolytic cleavage of H_2O_2 to hydroxyl radicals. Its effectiveness was further enhanced by the generation of hydroxyl radicals when exposed to visible light, making it operate as a catalyst similar to photo-Fenton. Magnetic Fe_3O_4 NPs facilitate the separation of the catalyst/photocatalyst following the reaction without affecting the catalytic/photocatalytic performance [67].

3.2. Heterojunction

Photocatalyst heterojunctions include amalgamating two or more distinct photocatalytic materials to create a junction that improves photocatalytic efficacy in destroying organic pollutants. The principal impetus for forming heterojunctions is to leverage the synergistic features of diverse materials, resulting in enhanced efficiency in light absorption, charge separation, and total photocatalytic efficacy. The fundamental principles of photocatalyst heterojunctions encompass charge carrier dynamics: electron–hole pairs are produced upon light absorption. The junction aids in segregating these charges, diminishing recombination rates and increasing the availability of charge carriers for chemical processes. The electronic band structures of the constituent components are essential. An advantageous band alignment (type II, p-n, etc.) can facilitate the effective transfer of electrons and holes between the elements. Materials frequently employed in forming photocatalyst heterojunctions comprise TiO_2, ZnO, CdS, g-C_3N_4, and metal oxides. Graphene and carbon nanotubes, as carbon-based materials, can improve charge conductivity. Various techniques can be utilized to fabricate heterojunctions, including hydrothermal or solvothermal procedures, sol–gel processes, and chemical vapor deposition.

Photocatalyst heterojunctions are promising for improving photocatalytic processes by combining semiconductors with different band gaps. They enhance light absorption, charge separation, and redox reaction kinetics. Type I heterojunctions promote electron–hole pairs, while type II heterojunctions create an internal electric field, preventing recombination and promoting redox reactions. Z-scheme heterojunctions combine type I and II, transferring electrons to holes through a redox mediator (Figure 7). Conventional type II heterojunctions reduce redox abilities, but Z-scheme heterojunctions have a distinct migration pattern, addressing these drawbacks while maintaining a high reactive capacity.

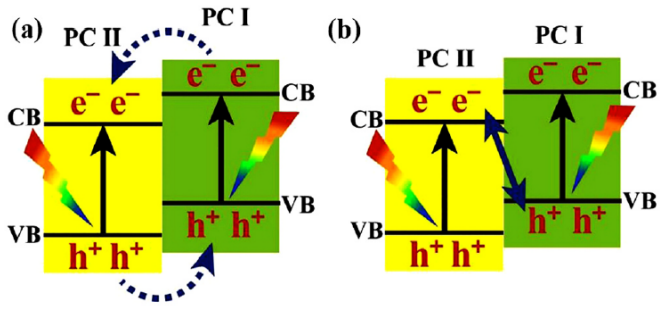

Figure 7. Schematic presentation of (**a**) type II-based and (**b**) direct Z-scheme heterojunctions [68].

Due to conventional type II and Z-heterojunction limitations, Yu et al. proposed a novel concept, the S-scheme heterojunction [69]. The S-concept consists of two n-type semiconductor photocatalysts, PC I, and PC II, representing oxidation and reduction photocatalysts, respectively (Figure 8b). A band-staggered combination of PC I and PC II forms the heterojunction. When the semiconductors come into contact, electrons flow spontaneously, bending photocatalysts B and A downward and upward. The internal electric field prevents electron migration, enhancing photocatalytic reaction efficiency [70].

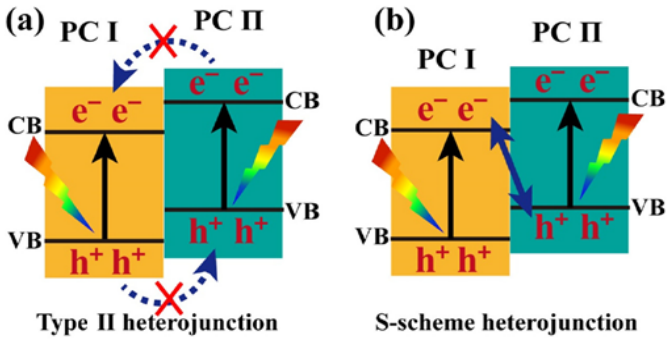

Figure 8. Schematic presentation of charge transfer in type II heterojunctions (**a**) and direct S-scheme (**b**) [69].

Hierarchical CeO_2@$Ni_{1-x}Co_xSe_2$ hollow spheres with an S-scheme heterojunction have been recently reported to exhibit rapid charge/mass transport, exceptional visible light absorption, superior activity, and excellent stability in photocatalytic CO_2 reduction with CO [71]. The photodegradation at the ZnO heterojunction was more efficient, occurring 300% and 33% faster than the individual Bi_2O_3 and ZnO catalysts, respectively, demonstrating a synergistic impact [72].

The selection of a synthesis technique for nano oxide particles is contingent upon the application's particular needs, encompassing particle size, morphology, distribution, purity, scalability, and cost factors. Researchers must evaluate these advantages and disadvantages to determine the suitable synthesis pathway for their intended use. Synthesis methods can vary widely, each offering advantages and disadvantages depending on the application, desired properties, and production scale. The pros and cons of the commonly applied methods can be summarized as follows. The sol–gel method offers controlled composition, homogeneity, and scalability for large-scale production. Still, it requires longer processing times and may require additional heat treatment. Coprecipitation is more straightforward, cost-effective, and quick but has limitations such as particle size control and potential contamination. Hydrothermal and solvothermal synthesis offers a high purity and crystalline quality but requires complex equipment and energy. Ball milling has scalability and versatility but has limitations like contamination, morphology control, and aggregation. Chemical vapor deposition produces high-purity and uniform materials but requires complex setups, high temperatures, and energy. It is suitable for thin-film applications but may require sophisticated setups and energy.

4. Metal Oxide Nanostructures and Photocatalytic Properties

4.1. TiO_2

Because of its cost-effectiveness and structural characteristics, TiO_2 (an *n*-type semiconductor) is the most intensively researched NMO for the photocatalytic breakdown of organic contaminants. With a broad energy band gap ranging from 3.0 to 3.2 eV, TiO_2 can only be stimulated by UV radiation. Hence, the utilization of visible light or sunshine is restricted.

The mechanisms of degradation of organic pollutants using TiO_2 as a photocatalyst proceed through the following steps: (a) adsorption onto the surface of TiO_2; (b) photocatalytic degradation by oxidation–reduction reactions, including photogenerated electrons, holes, and reactive species; and (c) desorption of the degradation outcomes. Organic dyes undergo degradation through two distinct pathways: (1) the indirect and (2) the direct pathway [73,74]:

1. The indirect pathway includes the indirect breakdown of dye molecules by generating potent oxidizing radicals following the absorption of UV radiation (Figure 9a). The degradation comprises several discrete steps. The first involves photon excitation of an electron from the valence band (VB) to the conduction band (CB) with energy equal to or

higher than the band gap energy (Eg), leading to an electron–hole (e^+/h^+) pair generation within the TiO_2:

$$TiO_2 + h\nu(UV) \rightarrow TiO_2(e^-(CB) + h^+(VB))$$

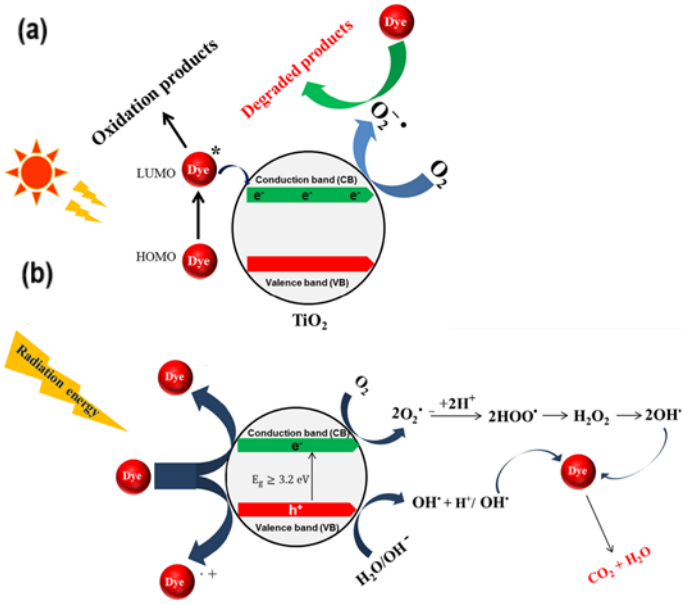

Figure 9. Schematic presentation of (**a**) indirect and (**b**) direct dye degradation mechanism on TiO_2 photocatalyst surface [74].

Moreover, photogenerated holes at VB produce OH• by reacting with adsorbed hydrogen formed by water ionization.

$$H_2O(ads) + h^+(VB) \rightarrow OH^{\cdot}(ads) + H^+(ads)$$

OH• radicals are potent oxidizing agents capable of chemically oxidizing organic molecules on the catalyst surface without selectivity, converting them into CO_2 and H_2O via mineralization. Then, electrons in the CB are captured by adsorbed oxygen, forming anionic superoxide radicals (O_2^-•).

$$O_2 + e^-(CB) \rightarrow O_2{-}(ads)$$

The involvement of the superoxide ion in the following oxidation processes relieves the recombination of electrons and holes, thereby preserving the electron neutrality of the TiO_2 material. Moreover, the superoxide ions react with hydrogen ions to produce hydroperoxyl radicals (HO_2•), which are then transformed into hydrogen peroxide (H_2O_2). The hydrogen peroxide subsequently decomposes to generate reactive OH•. Conventionally, oxidation and reduction occur on the surface of the photoexcited semiconductor photocatalyst, such as TiO_2.

$$2HOO^-(ads) \rightarrow H_2O_2(ads) + O_2$$

$$H_2O_2(ads) \rightarrow 2OH^-(ads)$$

$$Dye + OH^- \rightarrow CO_2 + H_2O \text{ (dye intermediates)}$$

$$Dye + h^+(VB) \rightarrow \text{oxidation products}$$

$$Dye + e^-(CB) \rightarrow \text{reduction products}$$

2. In the direct mechanism (Figure 9b), the excitation of dye molecules by visible light photons causes them to transition from their lowest energy state to an excited triplet state (refer to the equation below). The dye species that has been stimulated undergoes electron

transfer to the CV of TiO_2, converting it into a semi-oxidized radical cation (Dye + ϵ). Subsequently, the confined electrons react with the dissolved oxygen, forming superoxide radical anions (O_2^- ϵ), which produce hydroxyl radicals (OHϵ). The dominant role of these radicals is to oxidize organic molecules.

$$\text{Dye} + h\nu \rightarrow \text{Dye}^*$$

$$\text{Dye}^* + TiO_2 \rightarrow \text{Dye}^+ + TiO_2^-(CB)$$

$$TiO_2^-(CB) + O_2(ads) \rightarrow TiO_2 + O_2^-\bullet\,(ads)$$

$$\text{Dye} + O_2-\bullet\,(ads) \rightarrow \text{Degraded products}$$

Despite its efficacy in photocatalysis, TiO_2 has some disadvantages, which are outlined as follows [75]: (1) limitations in the transfer of electron and hole pairs, with the likely recombination of these charge carriers within TiO_2 leading to reduced photocatalytic activity; (2) slow photocatalytic degradation rates due to the low adsorption of organic pollutants on the TiO_2 surface; (3) the aggregation of TiO_2 nanoparticles, resulting from their instability, which prevents effective light absorption at the active sites; (4) increased light scattering caused by TiO_2 nanoparticles, which reduces photocatalytic activity; (5) difficulties in the recovery and regeneration of the spent TiO_2; and (6) the high band gap energy of the initial TiO_2 photocatalyst, which affects its energy efficiency compared to standard heterostructure photocatalysts.

Diverse methodologies have been explored to augment its photocatalytic efficiency, such as introducing metals or non-metals or simultaneously introducing many elements. TiO_2 exhibits semiconducting properties because its CB and VB consist of Ti 3d and O 2p orbitals. Introducing dopants alters its electrical structure, wide band gap, and inherent characteristics, leading to an expanded photoresponse within the visible spectrum. Both metal ions and non-metal ions can enhance TiO_2 photolytic performance. The doping of TiO_2 with noble metal ions, rare earth elements, and transition metals has been usually reported. Nevertheless, there have been limited studies on doping TiO_2 with alkali metal ions, mainly due to their unexplored hydrophilicity and photocatalytic activity. Given the higher cost of transition metals than alkali metals, recent research increasingly focuses on alkali (Li, Na, K, Rb)-doped TiO_2.

Lithium doping decreases the diameters of TiO_2 NPs and alters their surface chemical morphologies and structures. As-prepared photocatalysts with varying LiBr concentrations show significantly improved methylene blue degradation efficiency and photocatalytic activity under UV light [76]. Moreover, Li-doped TiO_2 NPs exhibit enhanced photocatalytic activity in methyl orange decomposition, causing the rutile crystal phase formation, lowering the temperature needed to transition from the anatase to rutile phase, and triggering a mixed-crystal phenomenon [77]. Anatase TiO_2 nanotubes can be tailored by Na doping at different concentrations, resulting in reduced band gaps that match the visible solar spectrum. These nanotubes show the higher photodegradation efficiency of methylene blue dye. An increased Ti^{4+} to Ti^{3+} reduction plays an active role in improving the photocatalytic efficiency of the samples [78]. Doping TiO_2 with K enhanced its optical properties. The spectra demonstrated minimal absorption for pure TiO_2 film in the visible region. The band edge of the doped film was moved towards lower energy at 437 nm, increasing absorption. The decrease in band gap was caused by a shift in the optical absorption from UV to visible light and an increase in film thickness. TiO_2 absorption extended well into the visible area in the presence of a K dopant [79]. Rb doping enables a decrease in the NPs' size, improving the distribution of Rb-TiO_2 nanoflakes and inhibiting the recombination of photogenerated holes and electrons. These result in a degradation rate of up to 93% during one hour [80].

Doping with alkaline earth metals also enhances TiO_2 photocatalytic activity. Mg-doped NPs have superior activity in methylene blue degradation due to reduced band gap energy and charge recombination [81]. Oxygen vacancies increase with Mg doping, which is attributed to the difference in electronegativity and ionic radius between Ti and

Mg. These vacancies act as electron acceptors, reducing the recombination rate of electron–hole pairs [82]. Ca-doped TiO_2 nanofibers improved performance in photodegrading rhodamine B. The substitution of Ti^{4+} ions with Ca^{2+} ions, coupled with the introduction of oxygen vacancies, reduces the recombination of electron–hole pairs, thereby improving the photocatalytic efficiency of the nanofibers. Sr-doped TiO_2 NPs are efficient in Brilliant Green degradation under solar light. Sr doping increased the mesoporosity and surface area, suppressing electron–hole pair recombination.

Non-metals like nitrogen, carbon, sulfur, iodine, and fluorine have been used as dopants for TiO_2, with nitrogen being particularly suitable due to its atomic size and low ionization energy. Nitrogen doping reduces the band gap and mitigates electron and hole recombination [83,84]. Sulfur doping enhances degradation efficiency, but the choice of sulfur sources and preparation methods significantly influences S-doping efficiency [85–88]. Cationic doping replaces Ti with S^{4+} or S^{6+}, while anionic doping replaces oxygen with S^{2-}. In cationic form, hydroxyl groups and photoinduced holes contribute to photocatalytic activity, while in the anionic, electrons and holes contribute equally to the photocatalytic process [86]. Carbon doping enables a photocatalyst to be effective under visible light. Introducing carbon enhances photocatalytic activity by creating a new impurity energy level above the valence band, reducing the band gap and allowing the photocatalyst to absorb visible light.

The synergism between polyaniline and the TiO_2 nanocomposite was examined as an electrode system for use in dye-sensitized solar cells, both in the dark and under illumination with various metal phthalocyanine dyes. Cobalt phthalocyanine dye demonstrated a superior conversion efficiency compared to the other phthalocyanine dyes studied [89].

The immobilization of TiO_2 NPs onto suitable materials is also efficient in obtaining a more effective and stable photocatalyst; owing to their structural characteristics, such as a high surface area, stability, non-toxicity, and natural abundance, clay minerals are widely used as supports. The degradation mechanism involves the adsorption of pollutant molecules, followed by degradation through reactive oxygen species. The nanocomposites' high porosity and extensive surface area enable the rapid conversion and mineralization of the pollutants. The interlayer cations in the clay capture electrons while allowing holes to participate in the oxidation process, reducing the recombination rate and thereby improving photocatalytic activity compared to pure TiO_2. Furthermore, the clay enhances the reusability of the photocatalyst by facilitating its separation from the reaction mixture. Various clay minerals, montmorillonite, bentonite, kaolinite, smectite, and vermiculite, efficiently support TiO_2 NPs [90–94].

4.2. ZnO

ZnO (an n-type semiconductor with a band gap of 3.37 eV) is recognized as an advantageous photocatalyst due to its high stability, non-toxicity, environmental friendliness, and cost-effectiveness [95,96]. However, its wide band gap and rapid recombination rate of electron–hole pairs limit its photocatalytic effectiveness. Doping with metals or non-metals, incorporating noble metals, combining it with narrow band gap semiconductors, or supporting ZnO on various solid materials overcomes these limitations. Ba^{2+} ions introduced into the ZnO structure increased the surface area 14 times and improved hydrophilicity [97]. A positive correlation was observed between the surface hydrophilicity and the increased defectivity of the doped sample (Figure 10). The increased affinity with water is crucial for the better photocatalytic activity of the doped sample over the undoped one. Moreover, doping with Ba reduced photo corrosion and enhanced the stability of the sample when exposed to radiation.

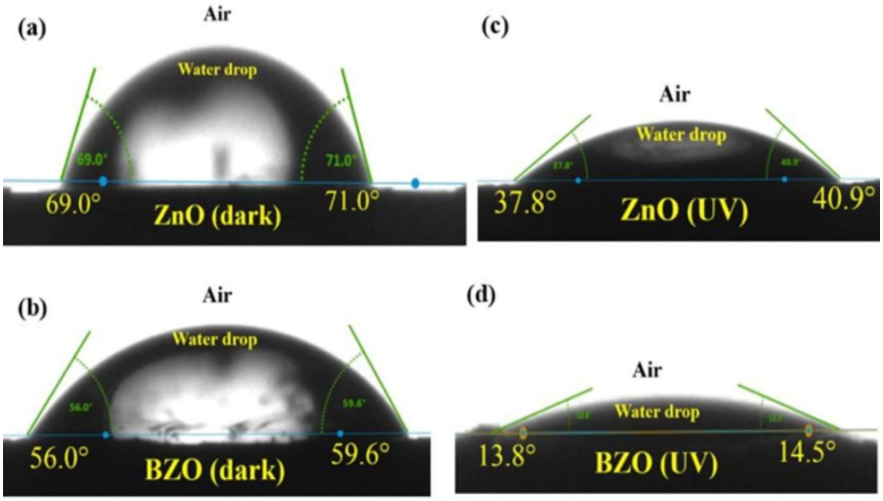

Figure 10. Shape of water drop on ZnO and Ba-doped ZnO (BZO) for static contact angle measurements in the dark (**a**,**b**) and after 10 min exposure to UV light irradiation (**c**,**d**) [97].

Doping ZnO with Fe creates sub-band states within its band gap, enhancing photocatalytic efficiency. The choice of doping element depends on electronegativity and the difference between dopant ionic radius and Zn^{2+} radius. Fe is a preferred element due to its chemical stability and ion radii. Fe-doped ZnO NPs showed efficacy as visible light-responsive photocatalysts [95,98]. Cr^{3+} has an ionic radius comparable to that of Zn^{2+}, which was utilized to synthesize highly efficient photocatalysts [99,100]. The observed efficacy is ascribed to the existence of Cr^{3+} and Cr^{2+}, which augment the surface oxygen vacancies and alter the band gap of ZnO [99,100]. A similar effect was reported for Mn^{2+} and Mn^{3+}, which substituted Zn^{2+} within the lattice of ZnO [101]. The presence of Ni^{2+} in the ZnO crystal lattice led to a distortion of the lattice due to the discrepancy in ionic radii between Ni and Zn cations. The distortion increased vacancy defects within the ZnO's structure, impacting its optical and photoluminescence properties [102].

A band gap analysis showed a notable band gap (Eg) reduction with increasing Ni concentrations in ZnO lattice ZnO [103]. The influence of Ni presence on the degradation of methylene blue under blue laser light irradiation was proved (Figure 11).

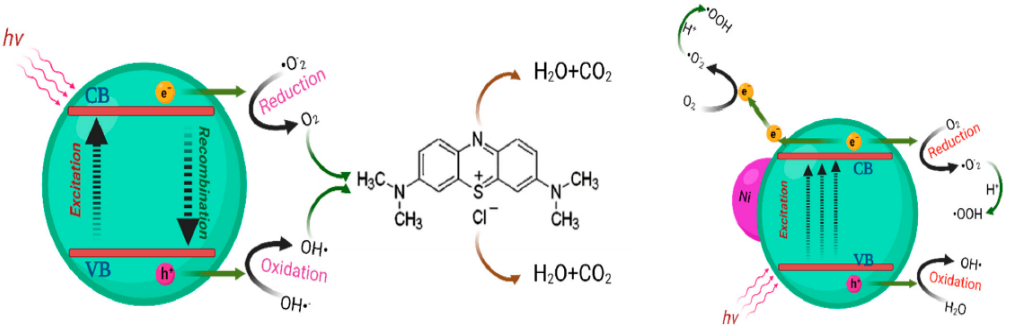

Figure 11. Diagram illustrating the impact of Ni doping on the ZnO nanostructure on the breakdown of methylene blue. Pure ZnO is on the left, and Ni-doped ZnO is on the right [103].

S-doped ZnO has an improved efficiency, which can be ascribed to an increased presence of oxygen vacancies. The photoactivity of ZnO doped with S and N was higher than that of C-doped ZnO in the degradation of methylene blue under UV–visible light. This behavior was attributed to the smaller crystallite size, lower band gap energy, and broader pore-size distribution resulting from S and N dopants [104].

The coupling of ZnO with other semiconductors to enhance its photocatalytic activity has also been explored. In this context, p-type oxides such as NiO and CuO are suitable for forming p–n heterojunctions with ZnO. This approach offers several benefits: (a) a

reduced recombination rate of electron–hole pairs; (b) the creation of narrow band gaps, which enhances visible light absorption; and (c) improved reusability with minimal loss in performance [105]. The primary mechanism for the enhanced photocatalytic activity is attributed to the more efficient separation of photogenerated charge carriers facilitated by the internal electric field at the ZnO/NiO interface. Photocatalytic studies conducted by Chen et al. revealed the formation of an internal electric field at the core–shell structure of the n-ZnO/p-NiO interface, which significantly enhanced the photocatalytic activity for the degradation of methylene blue under UV irradiation [106]. CuO/ZnO (Figure 12) involves various radical reactions, including N-deethylation, decarboxylation, deamination, dealkylation, chromophore cleavage, and ring-opening in the degradation process of Rhodamine B. It was suggested that $O_2\bullet^-$ is a crucial reactive species in the degradation process [107].

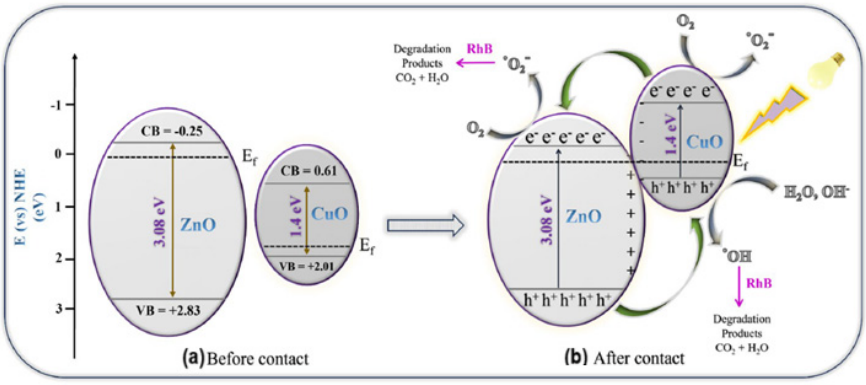

Figure 12. Schematic representation of the energy band diagram of the photodegradation process by CuO/ZnO nanocomposite [107].

The immobilization of ZnO NPs on porous materials like cellulose, clays, zeolites, and graphene oxides significantly enhances photocatalytic activity in reducing organic pollutants. The porous supports act as electron acceptors, improve adsorption, and generate oxygen vacancies in the ZnO lattice, extending its activity into the visible light spectrum. However, the ZnO content should be optimized to prevent aggregation [108–118].

4.3. CuO

CuO (a p-type semiconductor with a band gap of 1.2 to 2.1 eV) is effective in the visible range of the electromagnetic spectrum; however, its main drawback is the recombination between photogenerated electron–hole pairs, which reduces the efficiency of photocatalytic reactions. Zn-, Fe-, and Mn-doped CuO nanosheets are promising photocatalysts for the photodegradation of several organic dyes, since the doping induces a shift in the optical band gap, enhances visible light absorption, and reduces electron–hole recombination [119,120].

Combining CuO with other semiconductors yields an effective heterojunction material suitable for the photocatalytic degradation of different organic pollutants [121]. CuO/ZnO nanocomposites with a p–n heterojunction contribute to effectively separating the active charged ions, substantially reducing the recombination rate. A CuO/NiO photocatalyst with a p-p isotype heterojunction showed superior degradation activity under visible light due to superoxide and hydroxyl radicals, which are the primary reactive species involved in degradation [122,123].

CuO-supported graphene oxide has shown exceptional efficiency in reducing organic pollutants, thanks to synergistic effects with reduced graphene oxide properties [124]. The photocatalyst effectively degrades cationic methylene blue and anionic Congo red under visible light irradiation. Reduced graphene oxide creates a conductive network, enhancing charge transport. CuO-supported clays and clay minerals (bentonite, kaolinite, and montmorillonite) efficiently degrade several organics under sunlight [125–127]. Radicals

•O_2− and •OH are vital in the degradation process of cationic dye, methylene blue. The photocatalytic process involves dye adsorption by montmorillonite and CuO, facilitated by electrostatic attraction, Lewis's base interaction, and hydrogen bonding. Various cations in montmorillonite exchange with cationic dye, and metal complexation occurs between dye electron-rich functional groups and Al^{3+} from the montmorillonite skeleton (Figure 13).

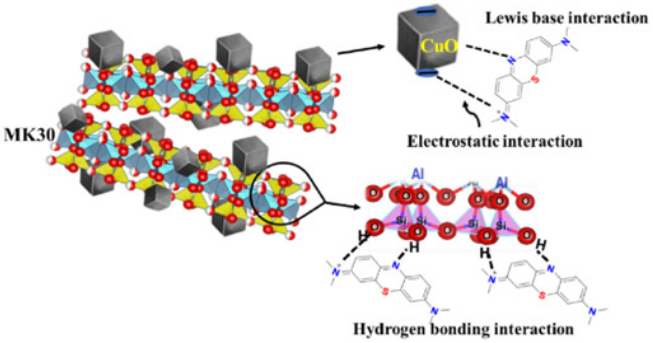

Figure 13. Schematic presentation of methylene blue degradation by CuO-supported montmorillonite [127].

4.4. Fe_2O_3

There are various kinds of iron oxide, including hematite (α-Fe_2O_3), maghemite (c-Fe_2O_3), and wustite (FeO). The most appealing mineral is hematite, α-Fe_2O_3. It has a small band gap energy of 2.1 eV and demonstrates excellent sensitivity to visible light. It is inexpensive, non-toxic, and chemically stable in water solutions. Its primary disadvantages are low electrical conductivity and absorptivity, leading to a high charge recombination and low photoactivity [128]. Additionally, the hydrophobic surface causes hydrophobic interactions between particles, promoting particle agglomeration and reducing the surface area [129]. Recently, it was reported that hematite impurities in clinoptilolite-rich tuff are responsible for the photolytic degradation of methylene blue under visible light [130].

Modifying the surface of Fe_2O_3 nanoparticles with Ag nanoparticles enhances their photocatalytic effectiveness in breaking down azo dyes under sunlight irradiation from 20% to 99%. Significantly, the Fe_2O_3 NPs doped with Ag are exceptionally stable and environmentally friendly, showing no signs of poisoning or photo-weathering [131]. The proposed photocatalytic process (Figure 14) involves the role of Ag NPs in capturing the photogenerated e− by acting as an electron absorber, therefore inhibiting charge conduction recombination.

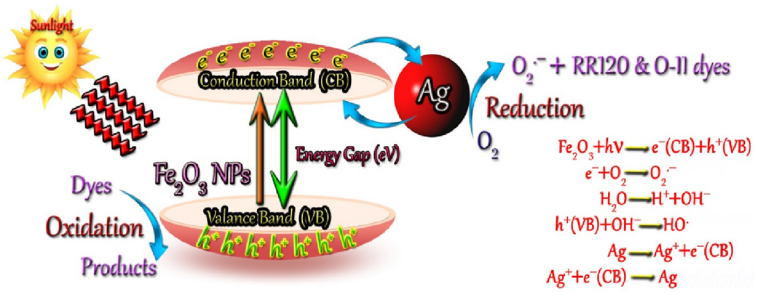

Figure 14. Mechanism of photocatalytic degradation of azo dyes using Ag–Fe_2O_3 NPs [131].

Ti- and Al-doped Fe_2O_3 exhibit significantly improved photocatalytic degradation of methyl orange compared to undoped Fe_2O_3 NPs [132]. The enhanced photocatalytic performance is attributed to grain refinement and the doping effect of Ti^{4+} and Al^{3+}. The Co(II) doping favors the growth of α-Fe_2O_3 and suppresses the growth of γ-Fe_2O_3. The doping narrows the band gap [133]. The doping of Cr(III) in α-Fe_2O_3 contributes to the ultrafast degradation of Congo red [134]. The doping of chromium influenced the significant factors responsible for the photocatalytic activity, the increase in range

of absorbance, increased e−/h+ pair separation, improvement in the charge transfer process, and active site formation, which significantly enhanced the degradation process. The optical band gap energy of α-Fe_2O_3 NPs slightly decreased after V^{4+} doping ions. Weak ferromagnetic behavior due to canted surface spins and the reduced coercivity and remanence after doping of V^{4+} ions is attributed to the creation of oxygen defects. Doped NPs showed a maximum of 92% photocatalytic degradation efficiency within 180 min. This was made possible by traps or defect states induced by V substitution, in addition to the band gap reduction of α-Fe_2O_3 NPs [135]. Moreover, incorporating Y^{3+} ions triggered the formation of novel energy levels [136]. The presence of d-level electrons in hematite can elevate the valence top, decreasing the optical band gap and increasing the absorption intensity of visible light. Excited electrons can readily transition from the VB to the conduction band (CB) and can be immediately absorbed by the energy level produced by Y^{3+}. Such action will impede the recombination of photogenerated electrons and holes, expediting the electron and hole separation process. Furthermore, the electrons will be transported to the surface of the photocatalyst to undergo a reaction with O_2 and generate $\bullet O^{2-}$ (Figure 15).

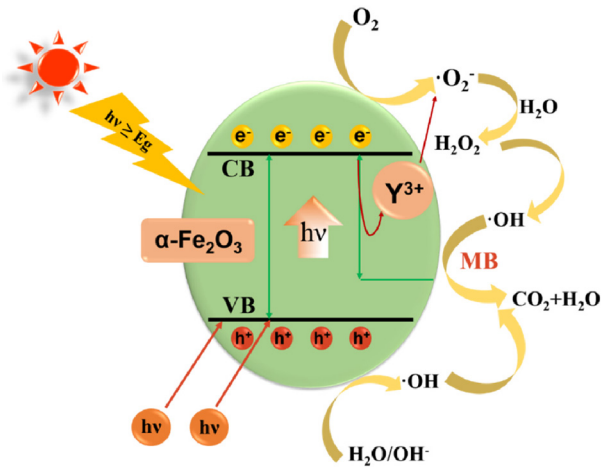

Figure 15. Photodegradation of methylene blue by Y-doped Fe_2O_3 [136].

In due course, more h+ ions will remain on VB to engage in reactions with H_2O molecules, resulting in the formation of •OH. This radical is widely recognized as the primary reactive species in the photocatalytic degradation process, improving the photocatalytic efficiency of hematite.

Recently, a theoretical study found that graphene-supported hematite with carbon vacancies has a nearly zero band gap, facilitating charge carrier transport to the surface. This improved carrier transport and catalysis benefit water splitting, a higher photocurrent density, and solar-driven water oxidation reactions [137].

4.5. Ag_2O

Silver(I) oxide (a p-type semiconductor) is receiving growing interest among semiconducting metal oxides. The narrow band gap (1.2 eV) of Ag_2O makes it well suited for application as a visible light photocatalyst. Yet, its sensitivity to light and fast recombination of electron–hole pairs generated by light significantly restrict its potential as a stable photocatalyst [138]. The morphology and dimensions of the particles modulate the photocatalytic characteristics of Ag_2O. The particle size can control the surface energy, resulting in a hydrophobic level or a superhydrophobic particle if the grain dimension meets roughness requirements. Ag_2O's wettability can be controlled by adjusting its crystal size during crystallization. Utilizing Ag_2O to photodecompose floating organic substances on the water surface is challenging. To overcome this, an attempt was made to prepare hydrophobic and oleophilic Ag_2O. The floatable superhydrophobic Ag_2O photocatalyst

can effectively treat oil-based pollution and avoid switchable wettability under sunlight irradiation [139]. Its stable superhydrophobic status under illumination allows it to be used in various real-world scenarios, including as a high-performance photocatalyst for local oil degradation.

The crystal study of Ag_2O revealed that surfaces (100), (110), and (111) are especially susceptible to damage, and alterations in their surface shape had a substantial impact on the oxide's activity [140]. Its photosensitivity and unstable nature limit the photocatalytic activity of Ag_2O in light, which leads to photoreduction, producing O_2 and Ag metal, diminishing its functionality [141].

Ag_2O/rectorite nanocomposites showed remarkable stability in photocatalytic degradation under visible and NIR light. The radical-trapping experiment revealed that $\bullet O_2^-$ is an active radical species participating in the photocatalytic breakdown of contaminants when exposed to visible light and NIR irradiation. The short energy band gap of Ag_2O in the nanocomposites resulted in a significant absorption of visible and NIR light during the degradation of dyes. The rectorite integrated into the nanocomposites offered highly effective active sites for the photo-adsorption process, enhanced electron and hole separation characteristics, and successfully prevented charge recombination [140].

4.6. SnO_2

At ambient temperature, tin oxide is a particular n-type metal oxide semiconductor with a band gap of 3.6 eV. It combines a high electrical conductivity and optical transparency. Having its qualities adjustable by size and shape alteration, it offers a broad variety of applications. It is extensively used as a gas sensor material because of its sensitivity to different gases [142]. Recently, SnO_2 NPs have been used for photocatalysis because of their lack of toxicity, environmentally friendly nature, and chemical stability [143]. Nevertheless, the effective implementation of SnO_2 nanoparticles as a photocatalyst is hindered by their broad band gap and elevated electron and hole recombination rate. The limited duration of electron and hole propagation diminishes the effectiveness of SnO_2 photodegradation. Due to its broadband gap, it exhibits reduced sensitivity to visible light-induced photocatalytic activity.

A recent investigation indicated that the photoluminescent properties of small nanoparticles (approximately 6 nm) are affected by the heating regime used during their production. The properties of SnO_2 dried at ambient conditions and SnO_2 dried under vacuum exhibit noteworthy differences. The former demonstrates more significant UV–Vis absorption throughout the range of wavelengths, a larger Urbach energy, and a smaller band gap, suggesting a higher concentration of defects ('Sn' vacancies). Vacuum drying effectively enhances the crystallinity of SnO_2. Considering its small energy gap and many defects, the first material demonstrates satisfactory degrading properties of methyl orange dye when exposed to UV and visible light [144]. Experimental studies show that the structural, electrical, and optical characteristics of SnO_2 alter by introducing foreign atoms (X—Fe, Pt, Sb, Zn, Bi, Mg, F, Mn, Eu^{3+}, Al, Ti, Co). Doped with various metals and transition metal ions, SnO_2 exhibits exceptional electrical, optical, and electrochemical activities. Surface flaws occur as a consequence of dopants reducing the band gap. Profound variations in lattice characteristics and the absorption peak result in substantial differences in X-ray diffraction patterns between doped and undoped SnO_2. Doped SnO_2 exhibits improved absorption capacity in the visible light spectrum due to incorporating flaws and oxygen vacancies through doping [145]. X-doped SnO_2 exhibits a distinct band gap compared to both pure SnO_2 and the dopant (x) because of their conduction band (CB) and valence band (VB) interaction. The conduction band (CB) and valence band (VB) in dopant and SnO_2 exhibit a band disposition determined by the specific band gap. The band gap of the x-doped SnO_2 composite promotes the efficient partitioning and movement of the electrons and holes produced by light absorption. Under visible light, the photogenerated electrons in an x-doped SnO_2 nanocomposite are stimulated from the valence band of the dopant and moved to the conduction band of SnO_2 [145]. The photogenerated holes, in contrast,

are stored in the VB. The extended lifespan of the excited electrons and holes is attributed to the transfer process (Figure 16B)). An expected consequence of electron transfer from the CB of SnO_2 to the CB of the doping material is inhibiting the reverse interaction between the photogenerated charge carriers (e^-/h^+). Recombination significantly reduces the photogenerated charge carriers, leading to photodegradation according to the method. The prevention of the recombination of photogenerated electron and hole pairs (e^-/h^+) can be achieved by doping SnO_2. This phenomenon enhances the photocatalytic efficiency of the photocatalyst when exposed to visible light. Upon rapid reaction, the electrons produce radicals that subsequently break down or oxidize the organic contaminants [145].

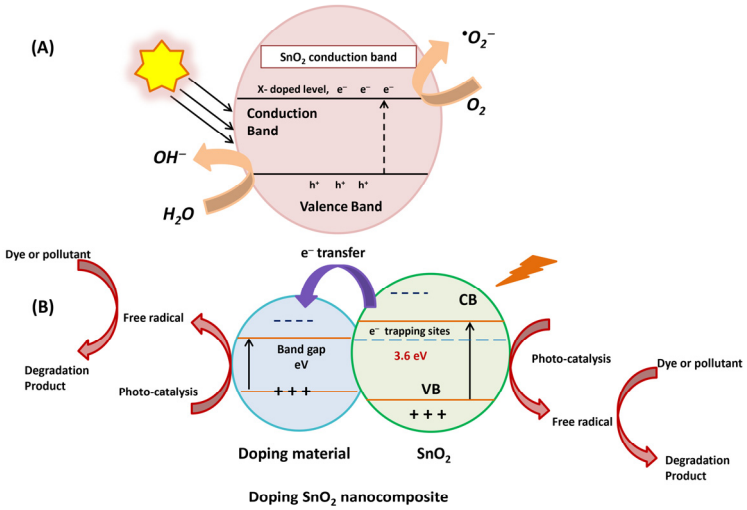

Figure 16. A schematic presentation of (**A**) the general mechanism of the SnO_2-based photocatalytic process and (**B**) the representation diagram of the electron transmission and the formation of degradation products by doped NPs [145].

For Fe-doped SnO_2, a recent report shows that doping causes (1) intermediate energy levels within the band gap created around the lower end of the conduction band; (2) this, in turn, enhances the separation of carriers and the dynamics of transformation; (3) the Fe-induced active sites play a crucial role in the adsorption and activation of the organic pollutant; (4) the oxygen vacancies have a role in both the adsorption and activation of O_2 and serve as dopant centers to decrease recombination and improve the separation of photoinduced electron–hole pairs [146].

Recent studies have shown that non-metal dopants, including nitrogen, carbon, sulfur, and fluorine, alter the band gap of SnO_2 by replacing the valence band, leading to an increase in oxygen vacancy defects on the nanoparticles' surface. Due to relatively small dimensions, C, F, O, and N diffuse through the lattice interstices and bind to the atoms via oxidation. Carbon is an ideal choice for non-metal dopants, particularly in semiconductors, due to its comparatively high mechanical strength, well-developed chemical resistance, and distinctive electrical characteristics. Moreover, doping can result in an increased generation of OH radicals, thereby enhancing the effectiveness of organic pollutant breakdown. This phenomenon can be elucidated because dopants will serve as electron hunters, thereby inhibiting the recombination of e^-/h^+ pairs. Consequently, the hole (h^+) of the photocatalyst will be liberated [147].

Doping the metal oxide with semiconductors of either a narrow or wide band gap can significantly improve its photocatalytic efficiency. Tin dioxide (SnO_2) semiconductors are extensively employed with TiO_2 semiconductors. A composite material consisting of SnO_2/TiO_2 nanotubes with different SnO_2 concentrations exhibited enhanced methylene blue absorption on the catalyst surface, leading to heightened metal oxide catalytic activity [148].

The surface modification of SnO_2 NPs can improve dispersion, luminescence, and mechanical properties. Chemical treatment with coupling agents affects the NPs' physical–chemical properties. Modified SnO_2 synthesized using grafting polymerization shows long-term durability and improved dispersion in the organic matrix. Ligand molecules are capping agents that prevent nanoparticle aggregation and control growth. Coating metal oxide nanoparticles with polymeric ligands improves their stability due to steric and electrostatic forces. However, the coating can also obstruct photocatalysis [149].

4.7. WO_3

Nano-structured WO_3 is a promising n-type semiconductor oxide because of its suitable band gap (2.6–2.8 eV), thus making it the second most searched photocatalyst activated under visible light. Due to its nontoxicity, affordability, high purity, long-lasting stability in different electrolytes, photosensitivity, and resistance to photo corrosion, it is of increasing interest. Compared to TiO_2 and ZnO, WO_3 offers benefits such as a more limited energy gap and a broader spectrum of light that can be absorbed. Its exceptional response properties to visible light, which constitutes over half of solar radiation energy, make it an ideal photocatalytic material. Metal–organic framework (WO_3) crystals are found in several forms, such as monoclinic, triclinic, orthorhombic, tetragonal, and hexagonal phases. At ambient temperature, monoclinic, triclinic, orthorhombic, and hexagonal phases are stable [150].

WO_3 has been extensively studied for its role in removing contaminants, reducing CO_2, and splitting water. However, the precise tuning of performance and morphology is necessary for specific applications [150]. Designing a WO_3-based photocatalyst tailored for each application could be essential for optimal effectiveness.

Modifying its morphology is crucial to enhancing WO_3 efficiency, and a comprehensive investigation is needed to understand the consequences of WO_3 morphological properties. Morphology plays an essential role in photocatalytic performance, as it exposes active crystal surfaces, increases surface area, and shortens transport distance. The regulation of morphology in photocatalytic materials is an effective policy that advances photocatalysis (Figure 17).

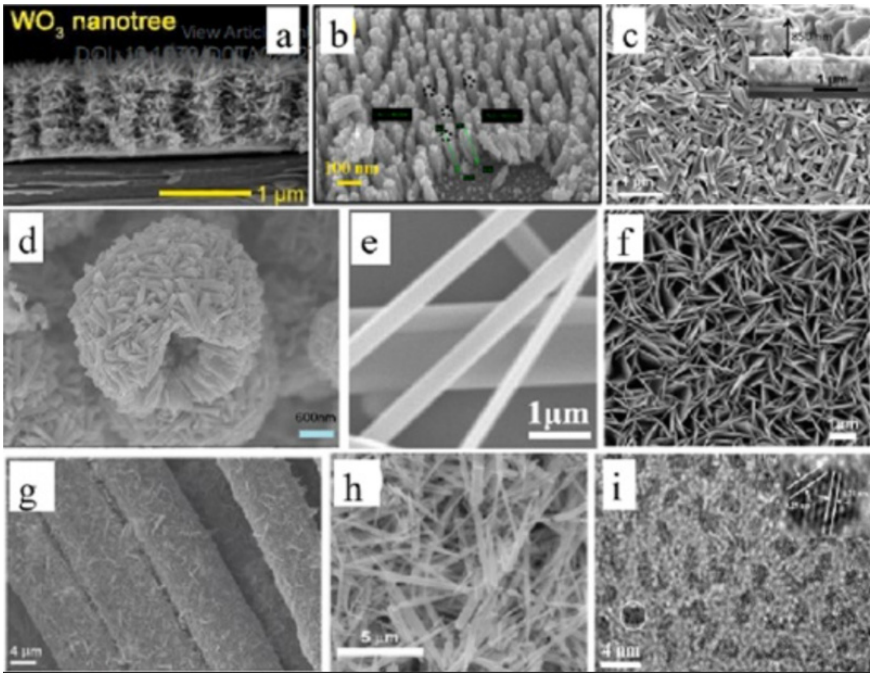

Figure 17. SEM images of different morphologies of WO_3 NPs: (**a**) nanotrees, (**b**) nanowires, (**c**) nanoplate array films, (**d**) hollow nest-like structure, (**e**) nanoroads, (**f**) nanosheets, (**g**) nanotubes, (**h**) needle-shaped nanorods, (**i**) quantum dots [150].

The surface properties significantly influence photocatalytic performance, with exposed crystal planes playing a crucial role in photocatalytic reactions. A near-perfect octahedron WO_3 was synthesized [151]. A thin tungstic acid layer covered this unique octahedron, significantly affecting its adsorption ability (Figure 18). The bounding {111} planes are likely not the lowest energy surfaces, and the tungstic acid covering helped stabilize the octahedron morphology. The as-prepared octahedra exhibits high visible-light-driven photocatalytic reducibility. They can remove Ag^+ ions in the photoprocessing of wastewater [151].

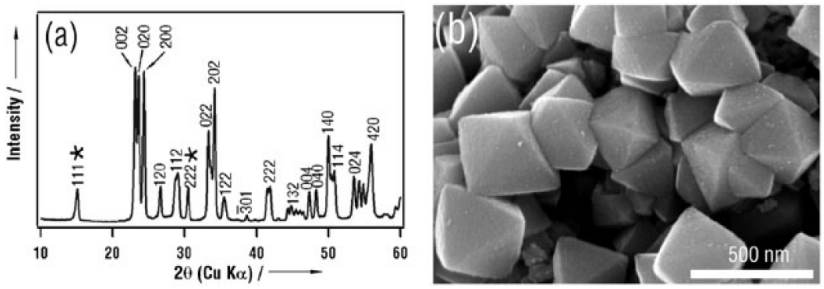

Figure 18. (**a**) XRD pattern and (**b**) SEM images of octahedral crystals (the asterisks represent diffractions corresponding to $H_2W_{1.5}O_{5.5}H_2O$) [151].

Moreover, doping is probably one of the most efficient approaches for enhancing WO_3 efficiency, improving light absorption, and reducing recombination rates. The electrocatalytic and photoelectrochemical activity of WO_3 changes non-monotonically with the Mn or V doping concentration due to local changes in the reduced nature of WO_3 and the formation of oxygen vacancies. The improved activity arises from fine-tuning the electronic structure and lessened free energy for atomic hydrogen adsorption. For photoelectrochemical water splitting, the photocurrent density increases from 0.61 mA cm^2 for the undoped WO_3 to about 1.38 mA cm^2 and 2.49 mA cm^2 for optimal Mn and V doping, respectively. Mn/V doping transforms WO_3 semiconductors into degenerate semiconducting materials with an improved metallic nature and suitable Gibbs-free energy [152].

Photocatalytic activity can also be enhanced by loading noble metals onto the WO_3. Although Au nanoparticles distributed on the WO_3 surface do not alter the selectivity of methylene blue photodegradation, they break methylene blue at a higher rate than the original WO_3 [68]. The increased photocatalytic activity has been ascribed to the improved separation of electron–hole pairs following the excitation of WO_3 at its band gap. Photogenerated holes in the CB of WO_3 are transported to Au, which has a lower Fermi level, under visible light. These holes directly contribute to methylene blue's oxidative degradation, boosting the photocatalyst's photocatalytic activity.

g-C_3N_4/CQDs/WO_3, a combination of graphite-like carbon nitride (g-C_3N_4), WO_3, and carbon quantum dots (CQDs) obtained by Z-scheme heterojunction, was tested for the depolymerization of lignin. The photocatalyst demonstrated a promising effect on depolymerizing four types of lignin, while effectively reducing the recombination rate of photogenerated carriers. The addition of CQDs expanded the light absorption range and improved the mobility of photogenerated carriers. An innovative approach for the highly selective cleavage of lignin C-C bonds was designed through heterojunction engineering [153].

A WO_3/Ag_3PO_4 composite showed improved photocatalytic performance and stability, ascribed to its direct Z-scheme heterojunction structure and the synergistic interaction between WO_3 and Ag_3PO_4. This combination enables the effective separation of electrons and holes and increases the conversion efficiency of light energy. Upon exposure to visible light, the photoexcited electrons in the CB of WO_3 and the retained holes in the valence band of Ag_3PO4 rapidly merge (Figure 19). Furthermore, the photogenerated holes in the VB of WO_3 greatly influence the oxidation reaction [154].

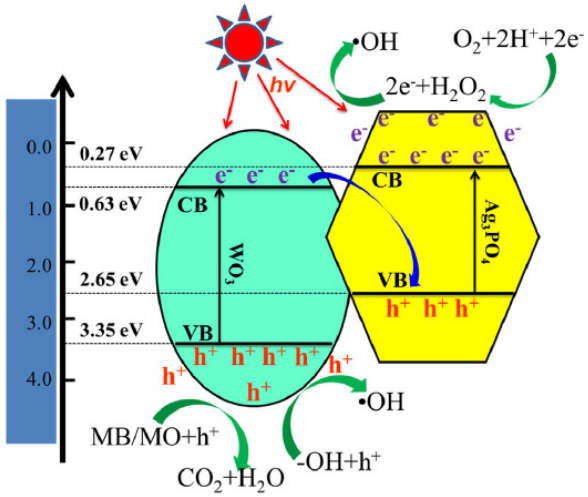

Figure 19. Proposed mechanism for the photodegradation of methylene blue (MB) and methyl orange (MO) in the direct Z-scheme charge carrier transfer process at the WO_3/Ag_3PO_4 composite interface [154].

Bare WO_3 displays a low photocatalytic performance because of the poor charge separation efficacy of its generated charge carriers. Graphene sheets are a promising material for charge transfer mechanisms. Reduced graphene oxide (RGO) enhances photogenerated electron transmission between graphene and MO semiconductors and enhances photocatalytic activity. A significant increase in O_2 production was reported for RGO/WO_3 compared to pristine WO_3 [155]. This improved the light absorption capability and utilization of electron–hole pairs in hybrid RGO/WO_3 nanoplates.

The photocatalytic effectiveness of the ternary photocatalyst (NH_2-GO/ZnO-WO_3) is superior in the degradation of several organic dyes when exposed to UV light. The improved photocatalytic efficiency mainly results from the low recombination rate of photoactive electron-hole pairs, the small energy band gap, and the extensive surface area of the ternary composite. Including lone pair electrons in the amino group forms a negatively charged surface composite. This, in turn, facilitates a favorable interaction with cationic dyes, which critically enhances the photocatalytic activity (Figure 20). The ternary nanocomposite NH_2-GO/ZnO-WO_3 has a suitable photocatalytic activity for degrading organic dyes often employed in industrial applications [156].

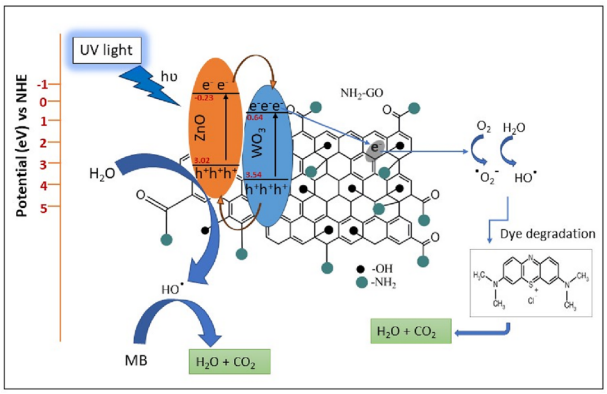

Figure 20. Schematic presentation of methylene blue (MB) photodegradation mechanism by NH_2-GO/ZnO-WO_3 composite [156].

A summary and comparison of the photocatalytic capabilities of various NMO-based photocatalysts are presented in Table 1.

Table 1. Photocatalytic properties of several NMO-based photocatalysts.

Photocatalyst	Model Pollutant	Operational Conditions (Light Type/C_0/Photocatalyst Amount)	Efficiency, %	Reaction Time, min	Reference
Rb-doped TiO_2	Methylene blue	UV light/10 ppm/0.4 g dm^{-3}	97	60	[80]
Ca-doped TiO_2	Rhodamine B	UV light/1 × 10^{-5} mol dm^{-3}/1.2 g dm^{-3}	95	100	[81]
TiO_2-pillared clay	Phenol	UV irradiation/50 ppm/2.0 g dm^{-3}	97.4	120	[93]
Fe-doped ZnO	Acid orange 7	Visible light/10 ppm/1.5 g dm^{-3}	52	180	[98]
Cu-Ni co-doped ZnO	Indigo carmine dye	Visible light/100 ppm/1 g dm^{-3}	93.3	60	[96]
CuO	Methylene blue Malachite green	Visible light/10 ppm/50 mg	62 70	270 30	[119]
Zn-CuO	Methylene blue Malachite green	Visible light/10 ppm/50 mg	66 85	270 30	[119]
Fe-CuO	Methylene blue Malachite green	Visible light/10 ppm/50 mg	66 90	270 30	[119]
Mn-doped CuO	Rhodamine B	Visible light/10 ppm/5 mg	93.8	90	[120]
CuO-ZnO	Tetracycline Ciprofloxacin	Natural sunlight/25 ppm/30 mg	94 93	50	[121]
CuO-NiO	Cefixime	Sunlight/15.22 ppm,/1 g dm^{-3}	90	180	[122]
CuO-montmorillonite 30	Methylene blue	Visible light/10 ppm/0.02 g dm^{-3}	98	40	[127]
Fe_2O_3	Orange-II Reactive red 120	Direct natural solar light irradiation/20 ppm/1 g dm^{-3}	23 20	120	[131]
Co-Fe_2O_3	Orange-II Reactive red 120	Direct natural solar light irradiation/20 ppm/1 g dm^{-3}	34 27	120	[131]
Cu–Fe_2O_3	Orange-II Reactive red 120 Orange-II Reactive red 120	Direct natural solar light irradiation/20 ppm/1 g dm^{-3}	81 71	120	[131]
Ag–Fe_2O_3	Orange-II Reactive red 120	Direct natural solar light irradiation/20 ppm/1 g dm^{-3}	97 99	120	[131]
Cr-Fe_2O_3	Congo red dye	Sunlight/30 ppm/30 mg dm^{-3}	95.2	15	[134]
Fe-SnO_2	Ciprofloxacin	UV light/10 ppm/50 mg	98.2	120	[146]
SnO_2-clinoptilolite	Methylene blue	Visible ligh/10 ppm/0.2 g dm^{-3}	45.0	180	[134]

4.8. Kinetics and Thermodynamics of Photodegradation

Kinetic studies on the photocatalytic degradation of organic compounds have been recorded in the literature, providing substantial evidence to clarify the process and its effectiveness. The Langmuir–Hinshelwood and pseudo-order kinetic models have frequently been assessed. The L–H model correlates effectively with the literature's experimental kinetic data about photocatalytic degradation. The photodegradation of methylene blue utilizing ZnO nanoparticles [157] indicated that the Langmuir–Hinshelwood model had a more favorable correlation with the experimental results than other models. The photodegradation of 2-chlorophenol using TiO_2 followed the Langmuir–Hinshelwood model, demonstrating a strong correlation coefficient (R^2 = 0.987) [158]. Moreover, the L–H model offered a more accurate representation than first-order kinetics for the photodegradation of amoxicillin using activated carbon-supported TiO_2 nanoparticles [159]. Tran et al. showed that only a limited number of research studies have successfully applied the pseudo-second model for photodegradation to date [160].

The thermodynamic driving force for photocatalysis is the alteration in Gibbs free energy (ΔG) of electron and hole systems in semiconductors due to light stimulation. Temperature does not influence the Gibbs free energy of semiconductors, so it cannot elicit the photocatalytic effect. A fundamental relationship between thermodynamics and kinetics is present in photocatalysis, with external factors such as organic species, light intensity, and temperature affecting the photocatalytic rate by influencing the thermodynamic driving force [161]. A recent investigation of the photodegradation of methylene blue by nanoparticles indicated that the reaction is spontaneous and endothermic [162], just as in the photodegradation of the dyes rhodamine B and alizarin R. The isotherm data were most accurately fitted to a Freundlich isotherm [163]. A recent study shows that photodegradation reactions facilitated by nickel manganite NPs are spontaneous and driven by entropy, advancing favorably at elevated temperatures [164].

5. Conclusions

Metal oxide-based photocatalyst systems have shown significant progress, but many challenges and opportunities remain to be explored. Most of the research on the photocatalysts is focused on powder materials. The synthesis of these powder materials in

large quantities is complicated, and their respective recycling for real-time applications is also quite tricky. Moreover, the toxicity of the intermediates in the reaction is not easily predictable.

A comprehensive understanding of the charge transport process is essential to improving the activity of NMO-based photocatalysts. Heterogeneous photocatalysis is considered viable for degrading organic pollutants more effectively than conventional approaches. However, significant efforts are needed to overcome challenges such as understanding degradation mechanisms and nanostructure development.

NMO photocatalysts face challenges such as deactivation, cost, scalability, photostability, and charge carrier dynamics. Regeneration usually requires harsh conditions or chemical treatments, while synthesis can be expensive, especially for rare or precious metals. Long-term usability is affected by UV or visible light irradiation, and the fast recombination of charge carriers can lower efficiency. Accordingly, future perspectives must include material innovation, doping and defect engineering, advances in synthesis techniques, and integration with other technologies. Expanding our understanding of photocatalytic mechanisms at the nanoscale and addressing potential environmental impacts are also crucial for a successful application. A deep understanding of active sites, carrier transport paths, and carrier life on surfaces, interfaces, and nanostructures is also necessary.

Finally, a further challenge lies in translating laboratory-level research on NMO NP-anchored photocatalysts into commercially viable tools to meet the requirements for the practical use of solar energy in environmental cleaning and renewable energy.

Author Contributions: Conceptualization, N.R.; methodology, N.R., J.P. and N.N.T.; writing—original draft preparation, N.R., J.P. and N.N.T.; writing—review and editing, N.R. and J.P.; visualization, N.R., J.P. and N.N.T.; supervision, N.R. All authors have read and agreed to the published version of the manuscript.

Funding: This research was funded by the Ministry of Science, Technological Development, and Innovation of the Republic of Serbia (Project number: 451-03-66/2024-03/200011) and the Slovenian Research and Innovation Agency (Research program P1-0418) and NETPORE COST action CA20126.

Data Availability Statement: The data are contained within the article.

Conflicts of Interest: The authors declare no conflicts of interest.

References

1. Zan, L.; Amin, H.M.A.; Mostafa, E.; Abd-El-Latif, A.A.; Iqbal, S.; Baltruschat, H. Electrodeposited cobalt nanosheets on smooth silver as a bifunctional catalyst for OER and ORR: In situ structural and catalytic characterization. *ACS Appl. Mater. Interfaces* **2022**, *14*, 55458–55470. [CrossRef]
2. Suherman, A.L.; Zampardi, G.; Kuss, S.; Tanner, E.E.L.; Amin, H.M.A.; Young, N.P.; Compton, R.G. Understanding gold nanoparticle dissolution in cyanide-containing solution via impact-chemistry. *Phys. Chem. Chem. Phys.* **2018**, *20*, 28300–28307. [CrossRef] [PubMed]
3. Akbari, A.; Amini, M.; Tarassoli, A.; Eftekhari-Sis, B.; Ghasemian, N.; Jabbari, E. Transition metal oxide nanoparticles as efficient catalysts in oxidation reactions. *Nano-Struct. Nano-Objects* **2018**, *14*, 19–48. [CrossRef]
4. Awogbemi, O.; Ojo, A.A.; Adeleye, S.A. Advancements in the application of metal oxide nanocatalysts for sustainable biodiesel production. *Discov. Appl. Sci.* **2024**, *6*, 250. [CrossRef]
5. Fazio, E.; Spadaro, S.; Corsaro, C.; Neri, G.; Leonardi, S.G.; Neri, F.; Lavanya, N.; Sekar, C.; Donato, N.; Neri, G. Metal-oxide based nanomaterials: Synthesis, characterization and their applications in electrical and electrochemical sensors. *Sensors* **2021**, *21*, 2494. [CrossRef] [PubMed]
6. Tejashwini, D.M.; Harini, H.V.; Nagaswarupa, H.P.; Naik, R.; Deshmukh, V.V.; Basavaraju, N. An in-depth exploration of eco-friendly synthesis methods for metal oxide nanoparticles and their role in photocatalysis for industrial dye degradation. *Chem. Phys. Impact* **2023**, *7*, 100355. [CrossRef]
7. Malato, S.; Fernández-Ibánez, P.; Maldonado, M.I.; Blanco, J.; Gernjak, W. Decontamination and disinfection of water by solar photocatalysis: Recent overview and trends. *Catal. Today* **2009**, *147*, 1–59. [CrossRef]
8. Zhu, S.; Wang, D. Photocatalysis: Basic Principles, Diverse Forms of Implementations and Emerging Scientific Opportunities. *Adv. Energy Mater.* **2017**, *7*, 17100841. [CrossRef]
9. Yang, X.; Wang, D. Photocatalysis: From fundamental principles to materials and applications. *ACS Appl. Energy Mater.* **2018**, *1*, 6657–6693. [CrossRef]

10. Ren, G.; Han, H.; Wang, Y.; Liu, S.; Zhao, J.; Meng, X.; Li, Z. Recent Advances of Photocatalytic Application in Water Treatment: A Review. *Nanomaterials* **2021**, *11*, 1804. [CrossRef]
11. Tamirat, A.G.; Rick, J.; Dubale, A.A.; Su, W.N.; Hwang, B.J. Using hematite for photoelectrochemical water splitting: A review of current progress and challenges. *Nanoscale Horiz.* **2016**, *1*, 243–267. [CrossRef] [PubMed]
12. Nasrollahi, N.; Ghalamchi, L.; Vatanpour, V.; Khataee, A. Photocatalytic-membrane technology: A critical review for membrane fouling mitigation. *J. Ind. Eng. Chem.* **2021**, *93*, 101–116. [CrossRef]
13. Araújo, E.S.; Pereira, M.F.G.; da Silva, G.M.G.; Tavares, G.F.; Oliveira, C.Y.B.; Faia, P.M. A Review on the use of metal oxide-based nanocomposites for the remediation of organics-contaminated water via photocatalysis: Fundamentals, bibliometric study and recent advances. *Toxics* **2023**, *11*, 658. [CrossRef]
14. Srivastava, S.K. Recent advances in removal of pharmaceutical pollutants in wastewater using metal oxides and carbonaceous materials as photocatalysts: A review. *RSC Appl. Interfaces* **2024**, *1*, 340–429. [CrossRef]
15. Krishnan, A.; Swarnalal, A.; Das, D.; Krishnan, M.; Saji, V.S.; Shibli, S.M.A. A review on transition metal oxides based photocatalysts for degradation of synthetic organic pollutants. *J. Environ. Sci.* **2024**, *139*, 389–417. [CrossRef]
16. Sun, J.; Jiang, C.; Wu, Z.; Liu, Y.; Sun, S. A review on the progress of the photocatalytic removal of refractory pollutants from water by BiOBr-based nanocomposites. *Chemosphere* **2022**, *308*, 136107. [CrossRef]
17. Danks, A.E.; Hall, S.R.; Schnepp, Z. The evolution of "sol–gel" chemistry as a technique for materials synthesis. *Mater. Horiz.* **2016**, *3*, 91–112. [CrossRef]
18. Moothedan, M.; Sherly, K.B. Surface properties of nano mesoporous lanthanum oxide synthesized by sol-gel method. *Mater. Today Proc.* **2022**, *66*, 2338–2341. [CrossRef]
19. Radhakrishna, S.K.C.; Meda, U.S. Synthesis of silicon di oxide nano-particles by sol-gel method for applications in geopolymer composites. *ECS Trans.* **2022**, *7*, 5533–5541. [CrossRef]
20. John, A.K.; Palaty, S. Influence of solvent and pH on the synthesis of visible light active titanium dioxide nano particles. *J. Sol-Gel Sci. Technol.* **2018**, *87*, 391–399. [CrossRef]
21. Rafiq, F.; Govindsamy, P.; Periyasamy, S. Synthesis of a novel nanoparticle $BaCoO_{2.6}$ through sol-gel method and elucidation of its structure and electrical properties. *J. Nanomater.* **2022**, *2022*, 3877879. [CrossRef]
22. Hasson, S.S.; Alsammarraie, A.M. Synthesis of nickel oxide nanoparticles by sol-gel method. *Int. J. Health Sci.* **2022**, *6*, 6915–6924. [CrossRef]
23. Althomali, R.H.; Adeosun, W.A. Wet chemically synthesized metal oxides nanoparticles, characterization and application in electrochemical energy storage: An updated review. *Synth. Met.* **2023**, *298*, 117424. [CrossRef]
24. Sharma, N.; Jha, R.; Jindal, N. Hydrothermally synthesized stannic oxide nano-hexagons. *Mater. Today Proc.* **2018**, *5*, 13807–13815. [CrossRef]
25. Suman, S.; Mukurala, N.; Kushwaha, A.K. Annealing induced surface restructuring in hydrothermally synthesized gallium oxide nano-cuboids. *J. Cryst. Growth* **2021**, *554*, 125946. [CrossRef]
26. Goel, R.; Jha, R.; Bhushan, M.; Bhardwaj, R.; Ravikant, C. Hydrothermally synthesized nickel oxide (NiO) nano petals. *Mater. Today Proc.* **2022**, *48*, 687–689. [CrossRef]
27. Liu, J.L.; Fan, L.Z.; Qu, X. Low temperature hydrothermal synthesis of nano-sized manganese oxide for supercapacitors. *Electrochim. Acta* **2012**, *66*, 302–305. [CrossRef]
28. Youssef, W.B.; Nefzi, H.; Sediri, F. Controlled and environmentally friendly hydrothermal synthesis of nano-V_4O_9 plate-like for photocatalytic degradation of methyl orange under solar irradiation. *Solid State Sci.* **2023**, *137*, 107126. [CrossRef]
29. Ali, K.; Sajid, M.; Bakar, S.A.; Younus, A.; Ali, H.; Rashid, M.Z. Synthesis of copper oxide (CuO) via coprecipitation method: Tailoring structural and optical properties of CuO nanoparticles for optoelectronic device applications. *Hybrid Advan.* **2024**, *6*, 100250. [CrossRef]
30. Mahmood, N.B.; Saeed, F.R.; Gbashi, K.R.; Mahmood, U.S. Synthesis and characterization of zinc oxide nanoparticles via oxalate co-precipitation method. *Mater. Lett. X* **2022**, *13*, 100126. [CrossRef]
31. Wu, N.; Wang, Y.; Liu, H.; Xiong, X. The influence of pH value on the synthesis of ytterbium silicate nano-powders by cocurrent coprecipitation method. *J. Non-Cryst. Solids* **2023**, *614*, 122407. [CrossRef]
32. Tan, Y.; Wang, Y.; Liu, H.; Xiong, X.; Cheng, H. Synthesis and high-temperature phase transformation behavior of Dy_2O_3–Sc_2O_3 co-stabilized ZrO_2 powders prepared by cocurrent chemical coprecipitation. *Ceram. Int.* **2024**, *50*, 22395–22404. [CrossRef]
33. Bao, Z.; Li, K.; Wang, S.; Gao, K.; Zhang, D.; Li, M. Preparation and characterization of submicron-cerium oxide by hypergravity coprecipitation method. *Adv. Powder Technol.* **2021**, *32*, 1611–1618. [CrossRef]
34. Kromer, M.L.; Monzó, J.; Lawrence, M.J.; Kolodziej, A.; Gossage, Z.T.; Simpson, B.H.; Morandi, S.; Yanson, A.; Rodríguez-López, J.; Rodríguez, P. High-throughput preparation of metal oxide nanocrystals by cathodic corrosion and their use as active photocatalysts. *Langmuir* **2017**, *33*, 13295–13302. [CrossRef] [PubMed]
35. Lawrence, M.J.; Kolodziej, A.; Rodriguez, P. Controllable synthesis of nanostructured metal oxide and oxyhydroxide materials via electrochemical methods. *Curr. Opin. Electroche.* **2018**, *10*, 7–15. [CrossRef]
36. Yang, Y.; Li, Y.; Pritzker, M. Control of Cu_2O film morphology using potentiostatic pulsed electrodeposition. *Electrochim. Acta* **2016**, *213*, 225–235. [CrossRef]
37. Atta, N.F.; Amin, H.M.A.; Khalil, M.W.; Galal, A. Nanotube arrays as photoanodes for dye sensitized solar cells using metal phthalocyanine dyes. *Int. J. Electrochem. Sci.* **2021**, *6*, 3316–3332. [CrossRef]

38. Cheng, H.; Wang, C.; Qin, D.; Xia, Y. Galvanic replacement synthesis of metal nanostructures: Bridgingthe gap between chemical and electrochemical approaches. *Acc. Chem. Res.* **2023**, *56*, 900–909. [CrossRef]
39. Oh, M.H.; Yu, T.; Yu, S.H.; Lim, B.; Ko, K.T.; Willinger, M.G.; Seo, D.H.; Kim, B.H.; Cho, M.G.; Park, J.H.; et al. Galvanic replacement reactions in metal oxide nanocrystals. *Science* **2013**, *340*, 964–968. [CrossRef]
40. Fitri, M.A.; Ota, M.; Hirota, Y.; Uchida, Y.; Hara, K.; Ino, D.; Nishiyama, N. Fabrication of TiO_2-graphene photocatalyst by direct chemical vapor deposition and its anti-fouling property. *Mater. Chem. Phys.* **2017**, *198*, 42–48. [CrossRef]
41. Cuong, T.M.; Tuan, V.A.; Linh, B.H.; Phuong, D.T.; Hoa, T.T.K.; Tuyen, N.D.; Tuan, N.Q.; Kosslick, H. Novel method for doping of nano TiO_2 photocatalysts by chemical vapor deposition. *Stud. Surf. Sci. Catal.* **2010**, *175*, 497–500. [CrossRef]
42. Zhao, D.; Sathasivam, S.; Li, J.; Carmalt, C.J. Transparent and conductive molybdenum-doped ZnO thin films via chemical vapor deposition. *ACS Appl. Electron. MA* **2020**, *2*, 120–125. [CrossRef]
43. Nagirnyak, S.V.; Lutz, V.A.; Donstova, T.A.; Astrelin, I.M. Synthesis and characterization of tin(IV) oxide obtained by chemical vapor deposition method. *Nanoscale Res. Lett.* **2016**, *11*, 343. [CrossRef]
44. Yu, J.; Kim, D. The preparation of nano size nickel oxide powder by spray pyrolysis process. *Powder Technol.* **2013**, *235*, 1030–1037. [CrossRef]
45. Kim, D.H.; Seo, D.J.; Yu, J.K. Application of spray pyrolysis process for the preparation of nano sized cobalt oxide powder. *Korean J. Mater. Res.* **2014**, *24*, 25–32. [CrossRef]
46. Fernández-Barahona, I.; Muñoz-Hernando, M.; Herranz, F. Microwave-driven synthesis of iron-oxide nanoparticles for molecular imaging. *Molecules* **2019**, *24*, 1224. [CrossRef]
47. Hasanpoor, M.; Aliofkhazraei, M.; Delavari, H. Microwave-assisted synthesis of zinc oxide nanoparticles. *Procedia Mater. Sci.* **2015**, *11*, 320–325. [CrossRef]
48. Falk, G.S.; Borlaf, M.; López-Muñoz, M.J.; Fariñas, J.C.; Rodrigues Neto, J.B.; Moreno, R. Microwave-assisted synthesis of TiO_2 nanoparticles: Photocatalytic activity of powders and thin films. *J. Nanopart. Res.* **2018**, *20*, 23. [CrossRef]
49. Zhang, M.; Wang, M.; Liu, X.; Huang, H.; Zhao, S.; Ma, J.; Liao, Y.; Li, X. Microwave-hydrothermal synthesis of F and Fe co-doped CeO_2 photocatalysts for efficient removal of 2,4,6-TCP under visible light. *Mat. Sci. Semicon. Proc.* **2024**, *171*, 108032. [CrossRef]
50. Arellano-Cortaza, M.; Ramírez-Morales, E.; Castillo, S.J.; Lartundo-Rojas, L.; Zamudio-Torres, I.; López Alejandro, E.M.; Rojas-Blanco, L. Microwave-assisted hydrothermal synthesis of type II ZnSe/ZnO heterostructures as photocatalysts for wastewater treatment. *Ceram. Int.* **2023**, *49*, 24027–24037. [CrossRef]
51. Lin, Y.R.; Chang, Y.C.; Ko, F.H. One-pot microwave-assisted synthesis of In_2S_3/In_2O_3 nanosheets as highly active visible light photocatalysts for seawater splitting. *Int. J. Hydrogen Energy* **2024**, *52*, 953–963. [CrossRef]
52. El-Naggar, M.E.; Wassel, A.R.; Shoueir, K. Visible-light driven photocatalytic effectiveness for solid-state synthesis of ZnO/natural clay/TiO_2 nanoarchitectures towards complete decolorization of methylene blue from aqueous solution. *Environ. Nanotechnol. Monit. Manag.* **2021**, *15*, 100425. [CrossRef]
53. Hu, J.; Cao, Y.; Xie, B.J.; Jia, D. Simple solid-state synthesis and improved performance of $Ni(OH)_2$-TiO_2 nanocomposites for photocatalytic H_2 production. *Ceram. Int.* **2017**, *43*, 11109–11115. [CrossRef]
54. Jadoun, S.; Arif, R.; Jangid, N.K.; Meena, R.K. Green synthesis of nanoparticles using plant extracts: A review. *Environ. Chem. Lett.* **2021**, *19*, 355–374. [CrossRef]
55. Ghaffar, S.; Abbas, A.; Naeem-ul-Hassan, M.; Assad, N.; Sher, M.; Ullah, S.; Alhazmi, H.A.; Najmi, A.; Zoghebi, K.; Al Bratty, M.; et al. Improved photocatalytic and antioxidant activity of olive fruit extract-mediated ZnO nanoparticles. *Antioxidants* **2023**, *12*, 1201. [CrossRef]
56. Ali, J.; Bibi, S.; Jatoi, W.B.; Tuzen, M.; Jakhrani, M.A.; Feng, X.; Saleh, T.A. Green synthesized zinc oxide nanostructures and their applications in dye-sensitized solar cells and photocatalysis: A review. *Mater. Today. Commun.* **2023**, *36*, 106840. [CrossRef]
57. Verma, V.; Al-Dossari, M.; Singh, J.; Rawat, M.; Kordy, M.G.M.; Shaban, M. A Review on green synthesis of TiO_2 NPs: Photocatalysis and antimicrobial applications. *Polymers* **2022**, *14*, 1444. [CrossRef] [PubMed]
58. Jha, A.K.; Prasad, K.; Kulkarni, A.R. Synthesis of TiO_2 nanoparticles using microorganisms. *Colloid. Surf. B* **2009**, *71*, 226–229. [CrossRef]
59. Haghighizadeh, A.; Aghababai Beni, A.; Haghmohammadi, M.; Samie, M.S.; Farshad, A.S. Green synthesis of ZnO-TiO_2 nano-photocatalyst doped with Fe(III) ions using bitter olive extract to treat textile wastewater containing reactive dyes. *Water Air Soil Pollut.* **2023**, *234*, 366. [CrossRef]
60. Singh, S.J.; Chinnamuthu, P. Highly efficient natural-sunlight-driven photodegradation of organic dyes with combustion derived Ce-doped CuO nanoparticles. *Colloid. Surf. A* **2021**, *625*, 126864. [CrossRef]
61. Giuffrida, F.; Calcagno, L.; Leonardi, A.A.; Cantarella, M.; Zimbone, M.; Impellizzeri, G. Enhancing the photocatalytic properties of doped TiO_2 nanowires grown by seed-assisted thermal oxidation. *Thin Solid Film.* **2023**, *771*, 139783. [CrossRef]
62. Serra-Pérez, E.; Dražić, G.; Takashima, M.; Ohtani, B.; Kovačič, S.; Žerjav, G.; Novak Tušar, N. Influence of the surface structure of the TiO_2 support on the properties of the Au/TiO_2 photocatalyst for water treatment under visible light. *Catal. Today* **2024**, *437*, 114764. [CrossRef]
63. Cravanzola, S.; Cesano, F.; Gaziano, F.; Scarano, D. Sulfur-doped TiO_2: Structure and surface properties. *Catalysts* **2017**, *7*, 214. [CrossRef]
64. Lin, L.Y.; Nie, Y.; Kavadiya, S.; Soundappan, T.; Biswas, P. N-doped reduced graphene oxide promoted Nano TiO_2 as a bifunctional adsorbent/photocatalyst for CO_2 photoreduction: Effect of N species. *Chem. Eng. J.* **2017**, *316*, 449–460. [CrossRef]

65. Perović, K.; Kovačić, M.; Kraljić Roković, M.; Kušić, H.; Genorio, B.; Lavrenčić Štangar, U.; Novak Tušar, N.; Lončarić Božić, A. The development of ternary-based TiO_2-SnS_2/GO-RGO composite material for photocatalytic H2 production under Solar light irradiation. *Mater. Res. Bull.* **2023**, *167*, 112418. [CrossRef]
66. Sen, P.; Bhattacharya, P.; Mukherjee, G.; Ganguly, J.; Marik, B.; Thapliyal, D.; Verma, S.; Verros, G.D.; Chauhan, M.S.; Arya, R.K. Advancements in doping strategies for enhanced photocatalysts and adsorbents in environmental remediation. *Technologies* **2023**, *11*, 144. [CrossRef]
67. Jorge López, J.; Reya, A.; Vinuelas-Zahinos, E.; Álvarez, P.M. Preparation of a new green magnetic Fe_3O_4 @TiO_2-P25 photocatalyst for solar advanced oxidation processes in water. *J. Environ. Chem. Eng.* **2023**, *11*, 109999. [CrossRef]
68. Dutta, V.; Sharma, S.; Raizada, P.; Thakur, V.K.; Khan, A.A.P.; Saini, V.; Asiri, A.M.; Singh, P. An overview on WO_3 based photocatalyst for environmental remediation. *J. Environ. Chem. Eng.* **2021**, *9*, 105018. [CrossRef]
69. Fu, J.; Xu, Q.; Low, J.; Jiang, C.; Yu, J. Ultrathin 2D/2D WO_3/g-C_3N_4 step-scheme H_2-production photocatalyst. *Appl. Catal. B-Environ.* **2019**, *243*, 556–565. [CrossRef]
70. Wang, Y.; Du, K.; Xu, R.; Cui, D.; Shi, Y.; Hao, W.; Du, Y. Bismuth-based semiconductor heterostructures for photocatalytic pollution gases removal. *Curr. Opin. Green Sust.* **2023**, *41*, 100824. [CrossRef]
71. Han, W.; Chen, Y.J.; Jiao, Y.Z.; Liang, S.M.; Li, W.; Tian, G.H. Oxygen vacancy-rich S-scheme CeO_2@$Ni_{1-x}Co_xSe_2$ hollow spheres derived from NiCo-MOF for remarkable photocatalytic CO_2 conversion. *ACS Sustain. Chem. Eng.* **2023**, *11*, 7787–7797. [CrossRef]
72. Shahzad, R.; Muneer, M.; Khalid, R.; Amin, H.M.A. ZnO-Bi_2O_3 Heterostructured composite for the Photocatalytic degradation of orange 16 reactive dye: Synergistic effect of UV irradiation and hydrogen peroxide. *Catalysts* **2023**, *13*, 1328. [CrossRef]
73. Ajmal, A.; Majeed, I.; Malik, R.N.; Idriss, H.; Nadeem, A. Principles and mechanisms of photocatalytic dye degradation on TiO_2 based photocatalysts: A comparative overview. *RSC Adv.* **2014**, *4*, 37003–37026. [CrossRef]
74. Nur, A.S.M.; Sultana, M.; Mondal, A.; Islam, S.; Robel, F.R.; Islam, A.; Sumi, M.S.A. A review on the development of elemental and codoped TiO_2 photocatalysts for enhanced dye degradation under UV–vis irradiation. *J. Water Process Eng.* **2022**, *47*, 102728. [CrossRef]
75. Chen, D.; Cheng, Y.; Zhou, N.; Chen, P.; Wang, Y.; Li, K.; Huo, S.; Cheng, P.; Peng, P.; Zhang, R.; et al. Photocatalytic degradation of organic pollutants using TiO_2-based photocatalysts: A review. *J. Clean. Prod.* **2020**, *268*, 121725. [CrossRef]
76. Guo, D.; Yi, J.; Sun, Y.; Zhou, H. Recent advances in titanium-based electrode materials for stationary sodium-ion batteries. *Energy Environ. Sci.* **2016**, *9*, 2978–3006. [CrossRef]
77. Zou, F.; Hu, J.; Miao, W.; Shen, Y.; Ding, J.; Jing, X. Synthesis and characterization of enhanced photocatalytic activity with Li+-doping nanosized TiO_2 catalyst. *ACS Omega* **2020**, *5*, 28510–28516. [CrossRef]
78. Rahman, H.; Norbert, A.; Nair, P.S.; Joseph, J.A.; Shaji, S.; Deshpande, U.; Naduvath, J.; Shanu, A.S.; Philip, R.R. Influence of sodium doping on the material properties and photocatalytic activity of anatase titanium dioxide nanotubes prepared by anodization. *Opt. Mater.* **2022**, *134*, 113172. [CrossRef]
79. Amna, H.; Kayani, Z.N.; Anwar, M. Effect of Au ions on structural, optical, magnetic, dielectric, and antibacterial properties of TiO_2 dip-coated thin films. *J. Mater. Sci. Mater. Electron.* **2021**, *32*, 14398–14419. [CrossRef]
80. Jia, L.; Yang, L.M.; Wang, W.; Huang, S.T.; Xu, Z. Preparation and characterization of Rb-doped TiO_2 powders for photocatalytic applications. *Rare Met.* **2024**, *43*, 555–561. [CrossRef]
81. Minchi, L.; Cao, F.; Xinni, Z.; Youqiang, C.; Xuhua, L. Photocatalytic activity of Ca-TiO_2 nanofibers with different concentrations of calcium. *Chem. Phys. Lett.* **2019**, *736*, 1363807. [CrossRef]
82. Nair, S.B.; Aijo, J.K.; Joseph, J.A.; Shaji, S.; Philip, R.R. Role of magnesium doping for ultrafast room temperature crystallization and improved photocatalytic behavior of TiO_2 nanotubes. *Mater. Today Proc.* **2020**, *25*, 203–207. [CrossRef]
83. Ansari, S.A.; Khan, M.M.; Ansari, M.O.; Cho, M.H. Nitrogen-doped titanium dioxide (N-doped TiO_2) for visible light photocatalysis. *New J.Chem.* **2016**, *40*, 3000. [CrossRef]
84. Bakre, P.V.; Tilve, S.G.; Shirsat, R.N. Influence of N sources on the photocatalytic activity of N-doped TiO_2. *Arab. J. Chem.* **2020**, *13*, 7637–7651. [CrossRef]
85. Ohno, T.; Akiyoshi, M.; Umebayashi, T.; Asai, K.; Mitsui, T.; Matsumura, M. Preparation of S-doped TiO_2 photocatalysts and their photocatalytic activities under visible light. *Appl. Catal. A Gen.* **2004**, *265*, 115–121. [CrossRef]
86. Bakar, S.A.; Ribeiro, C. A comparative run for visible-light-driven photocatalytic activity of anionic and cationic S-doped TiO_2 photocatalysts: A case study of possible sulfur doping through chemical protocol. *J. Mol. Catal. A-Chem.* **2016**, *421*, 1–15. [CrossRef]
87. Piątkowska, A.; Janus, M.; Szymański, K.; Mozia, S. C-,N- and S-Doped TiO_2 Photocatalysts: A Review. *Catalysts* **2021**, *11*, 144. [CrossRef]
88. Ahmadpour, N.; Nowrouzi, M.; Avargani, V.M.; Sayadi, M.H.; Zendehboudi, S. Design and optimization of TiO_2-based photocatalysts for efficient removal of pharmaceutical pollutants in water: Recent developments and challenges. *J. Water Process Eng.* **2024**, *57*, 104597. [CrossRef]
89. Atta, F.N.; Galal, A.; Amin, H.M.A. Synthesis and photoelectrochemical behavior of a hybrid electrode composed of polyaniline encapsulated in highly ordered TiO_2 nanotubes array. *Int. J. Electrochem. Sci.* **2012**, *7*, 3610–3626. [CrossRef]
90. Zhang, Y.; Miao, B.; Chen, Q.; Bai, Z.; Cao, Y.; Davaa, B. Synthesis, structure, and photocatalytic activity of TiO_2-montmorillonite composites. *Catalysts* **2022**, *12*, 486. [CrossRef]

91. Liu, J.; Dong, M.; Zuo, S.; Yu, Y. Solvothermal preparation of TiO_2/montmorillonite and photocatalytic activity. *Appl. Clay Sci.* **2009**, *43*, 156–159. [CrossRef]
92. Chen, D.; Zhu, H.; Wang, X. A facile method to synthesize the photocatalytic TiO_2/montmorillonite nanocomposites with enhanced photoactivity. *Appl. Surf. Sci.* **2014**, *319*, 158–166. [CrossRef]
93. Wang, G.; Yan, Y.; Yang, Y.; Li, J.; Gao, H.; Wang, J.; Zheng, X.; Yang, J. In situ synthesis of TiO_2-pillared bentonite photocatalyst and its enhanced photocatalytic performance. *Water Air Soil Pollut.* **2022**, *233*, 494. [CrossRef]
94. Kassir, M.; Roques-Carmes, T.; Pelletier, M.; Bihannic, I.; Alem, H.; Hamieh, T.; Toufaily, J.; Villiéras, F. Adsorption and photocatalysis activity of TiO_2/bentonite composites. *Desalin. Water Treat.* **2017**, *98*, 196–215. [CrossRef]
95. Srinivasulu, T.; Saritha, K.; Ramakrishna Reddy, K.T. Synthesis and characterization of Fe-doped ZnO thin films deposited by chemical spray pyrolysis. *Mod. Electron. Mater.* **2017**, *3*, 76–85. [CrossRef]
96. Kumar, R.; Gedam, R.S. Synthesis and characterization of bi-functional Cu and Ni co-doped ZnO photocatalysts for organic pollutant degradation and antimicrobial activity. *Ceram. Int.* **2024**, *50*, 24716–24724. [CrossRef]
97. Hamrouni, A.; Moussa, M.; Fessi, N.; Palmisano, L.; Ceccato, R.; Rayes, A.; Parrino, F. Solar photocatalytic activity of Ba-doped ZnO nanoparticles: The role of surface hydrophilicity. *Nanomaterials* **2023**, *13*, 2742. [CrossRef]
98. Mancuso, A.; Sacco, O.; Mottola, S.; Pragliola, S.; Moretta, A.; Vaiano, V.; De Marco, I. Synthesis of Fe-doped ZnO by supercritical antisolvent precipitation for the degradation of azo dyes under visible light. *Inorg. Chim. Acta.* **2023**, *549*, 121407. [CrossRef]
99. Chang, C.J.; Yang, T.L.; Weng, Y.C. Synthesis and characterization of Cr-doped ZnO nanorod-array photocatalysts with improved activity. *J. Solid State Chem.* **2014**, *214*, 101–107. [CrossRef]
100. Mathai, J.; Jose, A.K.; Anjana, M.P.; Aleena, P.A.; Kunjumon, J.; Ittyachan, R.; Nair, S.S.; Vinithad, G.; Sajan, D. Substantial effect of Cr doping on the third-order nonlinear optical properties of ZnO nanostructures. *Opt. Mater.* **2023**, *142*, 114128. [CrossRef]
101. Aadnan, I.; Zegaoui, O.; El Mragui, A.; Daou, I.; Moussout, H.; Esteves da Silva, J.C.G. Structural, Optical and Photocatalytic properties of Mn doped ZnO nanoparticles used as photocatalysts for azo-dye degradation under visible light. *Catalysts* **2022**, *12*, 1382. [CrossRef]
102. Lins, A.; Jerônimo, A.G.; Barbosa, R.; Neves, L.; Trigueiro, P.; Almeida, L.C.; Osajima, J.A.; Pereira, F.A.; Peña-Garcia, R.R. Facile Synthesis of Ni-doped ZnO nanoparticles using cashew gum: Investigation of the structural, optical, and photocatalytic properties. *Molecules* **2023**, *28*, 7772. [CrossRef]
103. Zyoud, S.H.; Ganesh, V.; Che Abdullah, C.A.; Yahia, I.S.; Zyoud, A.H.; Abdelkader, A.F.I.; Daher, M.G.; Nasor, M.; Shahwan, M.; Zahran, H.Y.; et al. Facile synthesis of Ni-doped ZnO nanostructures via laser-assisted chemical bath synthesis with high and durable photocatalytic activity. *Crystals* **2023**, *13*, 1087. [CrossRef]
104. Joy, A.; Viswanathan, M.R.; Vijayan, B.K.; Silva, C.G.; Basheer, I.; Sugathan, S.; Mohamed, P.A.; Solaiappan, A.; Shereef, A. Solar photocatalysts: Non-metal (C, N, and S)-doped ZnO synthesized through an industrially sustainable in situ approach for environmental remediation applications. *RSC Adv.* **2024**, *14*, 21655–21667. [CrossRef] [PubMed]
105. Thampy, U.S.U.; Mahesh, A.; Sibi, K.S.; Jawahar, I.N.; Biju, V. Enhanced photocatalytic activity of ZnO–NiO nanocomposites synthesized through a facile sonochemical route. *SN Appl. Sci.* **2019**, *1*, 1478. [CrossRef]
106. Chen, Z.; Dedova, T.; Spalatu, N.; Maticiuc, N.; Rusu, M.; Katerski, A.; Acik, I.O.; Unold, T.; Krunks, M. ZnO/NiO heterostructures with enhanced photocatalytic activity obtained by ultrasonic spraying of a NiO shell onto ZnO nanorods. *Colloids Surf. A Physicochem. Eng. Asp.* **2022**, *648*, 129366. [CrossRef]
107. Jeevarathinam, M.; Asharani, I.V. Synthesis of CuO, ZnO nanoparticles, and CuO-ZnO nanocomposite for enhanced photocatalytic degradation of Rhodamine B: A comparative study. *Sci. Rep.* **2024**, *14*, 9718. [CrossRef]
108. Li, X.; Zhang, L.; Wang, Z.; Wu, S.; Ma, J. Cellulose controlled zinc oxide nanoparticles with adjustable morphology and their photocatalytic performances. *Carbohyd. Polym.* **2021**, *259*, 117752. [CrossRef]
109. Shi, C.; An, B.; Zhang, L.; Zai, Z.; Shi, Z.; Wang, Z.; Ma, J. Contribution of surface carboxyl of cellulose in the formation mechanism and interfacial catalysis activity of ZnO/cellulose nanocomposites. *Appl. Surf. Sci.* **2023**, *618*, 156633. [CrossRef]
110. Ehsan, M.F.; Barai, H.R.; Islam, M.M.; Susan, M.A.B.H.; Joo, S.W.; Miran, M.S. ZnO nanocomposites supported by acid-activated kaolinite as photocatalysts for the enhanced photodegradation of an organic dye. *Mater. Today Commun.* **2023**, *36*, 106563. [CrossRef]
111. Haounati, R.; Ighnih; Malekshah, R.E.; Alahiane, S.; Alakhras, F.; Alabbad, E.; Alghamdi, H.; Ouachtak, H.; Addi, A.A.; Jada, A. Exploring ZnO/Montmorillonite photocatalysts for the removal of hazardous RhB Dye: A combined study using molecular dynamics simulations and experiments. *Mater. Today Commun.* **2023**, *35*, 105915. [CrossRef]
112. Iazdani, F.; Nezamzadeh-Ejhieh, A. The photocatalytic rate of ZnO supported onto natural zeolite nanoparticles in the photodegradation of an aromatic amine. *Environ. Sci. Pollut. Res.* **2021**, *28*, 53314–53327. [CrossRef]
113. Nezamzadeh-Ejhieh, A.; Khodabakhshi-Chermahini, F. Incorporated ZnO onto nano clinoptilolite particles as the active centers in the photodegradation of phenylhydrazine. *J. Ind. Eng. Chem.* **2014**, *20*, 695–704. [CrossRef]
114. Bahrami, M.; Nezamzadeh-Ejhieh, A. Effect of the supported ZnO on clinoptilolite nano-particles in the photodecolorization of semi-real sample bromothymol blue aqueous solution. *Mater. Sci. Semicond. Process.* **2015**, *30*, 275–284. [CrossRef]
115. De Dios, F.S.; Morales, E.R.; Cortaza, M.D.A.; Hernández, G.P.; Mandujano, E.V.M.; Alejandro, E.M.L.; Blanco, L.R. Improvement of photocatalysis using ZnO/zeolite nanocomposites for contaminant removal in aqueous media. *Desalin. Water Treat.* **2023**, *312*, 79–88. [CrossRef]

116. Da Silvaa, P.L.; Nippes, R.P.; Macruz, P.D.; Hegetob, F.L.; Scaliante, M.H.N.O. Photocatalytic degradation of hydroxychloroquine using ZnO supported on clinoptilolite zeolite. *Water Sci. Technol.* **2021**, *84*, 764. [CrossRef]
117. Abd-Elrahim, A.G.; Chun, D.M. Room-temperature deposition of ZnO-graphene nanocomposite hybrid photocatalysts for improved visible-light-driven degradation of methylene blue. *Ceram. Int.* **2021**, *47*, 12812–12825. [CrossRef]
118. Mirikaram, N.; Pérez-Molina, Á.; Morales-Torres, S.; Salemi, A.; Maldonado-Hódar, F.J.; Pastrana-Martinez, L.M. Photocatalytic perfomance of ZnO-graphene oxide composites towards the degradation of vanillic acid under solar radiation and visible-LED. *Nanomaterials* **2021**, *11*, 1576. [CrossRef]
119. Tank, R.; Seling, T.R.; Katzbaer, R.R.; Thompson, K.L.; Aksoy, S.E.; Chitara, B.; Shringi, A.K.; Schaak, R.E.; Riaz, U.; Yan, F. Transition metal-doped CuO nanosheets for enhanced visible-light photocatalysis. *J. Photoch. Photobio A* **2024**, *448*, 115356. [CrossRef]
120. Tamam, N.; Aadil, M.; Hassanc, W.; Ejaz, S.R.; Najm, Z.M.; Alsafari, I.A.; Aman, S.; Trukhanov, A.V.; Al-Buriahi, M.S.; Boukhris, I. Surfactant assisted synthesis of nanostructured Mn-doped CuO: An efficient photocatalyst for environmental remediation. *Ceram. Int.* **2022**, *48*, 29589–29600. [CrossRef]
121. Bano, K.; Kaushal, S.; Lal, B.; Joshi, S.K.; Kumar, R.; Singh, P.P. Fabrication of CuO/ZnO heterojunction photocatalyst for efficient photocatalytic degradation of tetracycline and ciprofloxacin under direct sun light. *Environ. Nanotechnol. Monit. Manag.* **2023**, *20*, 100863. [CrossRef]
122. Ul Rahman, Z.; Shah, U.; Alam, A.; Shah, Z.; Shaheen, K.; Bahadar Khan, S.; Ali Khan, S. Photocatalytic degradation of cefixime using CuO-NiO nanocomposite photocatalyst. *Inorg. Chem. Commun.* **2023**, *148*, 110312. [CrossRef]
123. Muhambihai, P.; Rama, V.; Subramaniam, P. Photocatalytic degradation of aniline blue, brilliant green and direct red 80 using NiO/CuO, CuO/ZnO and ZnO/NiO nanocomposites. *Environ. Nanotechnol. Monit. Manag.* **2020**, *14*, 100360. [CrossRef]
124. Sagadevan, S.; Lett, J.A.; Weldegebrieal, G.K.; Garg, S.; Oh, W.-C.; Hamizi, N.A.; Johan, M.R. Enhanced photocatalytic activity of rGO-CuO nanocomposites for the degradation of organic pollutants. *Catalysts* **2021**, *11*, 1008. [CrossRef]
125. Sohrabnezhad, S.; Takas, M.E. Synthesis and characterization of porous clay heterostructure intercalated with CuO nanoparticles as a visible light-driven photocatalyst. *J. Iran. Chem. Soc.* **2019**, *16*, 45–55. [CrossRef]
126. Yang, C.; Xu, H.; Shi, J.; Liu, Z.; Zhao, L. Preparation and photocatalysis of CuO/Bentonite based on adsorption and photocatalytic activity. *Materials* **2021**, *14*, 5803. [CrossRef]
127. Chellapandi, T.; Madhumitha, G.; Avinash, J. Ultrasonication-assisted synthesis of CuO-decorated montmorillonite K30 nanocomposites for photocatalytic removal of emerging contaminants: A response surface methodology approach. *Environ. Res.* **2024**, *259*, 119574. [CrossRef]
128. Han, S.; Hu, L.; Liang, Z.; Wageh, S.; Al-Ghamdi, A.A.; Chen, Y.; Fang, X. One-step hydrothermal synthesis of 2D hexagonal nanoplates of α-Fe_2O_3/graphene composites with enhanced photocatalytic activity. *Adv. Funct. Mater.* **2014**, *36*, 5719–5727. [CrossRef]
129. Choi, Y.W.; Lee, H.; Song, Y.; Sohn, D. Colloidal stability of iron oxide nanoparticles with multivalent polymer surfactants. *J. Colloid. Interf. Sci.* **2015**, *443*, 8–12. [CrossRef] [PubMed]
130. Pavlović, J.; Šuligoj, A.; Opresnik, M.; Tušar, N.N.; Logar, N.Z.; Rajić, N. Studies of clinoptilolite-rich zeolitic tuffs from different regions and their activity in photodegradation of methylene blue. *Catalysts* **2022**, *12*, 224. [CrossRef]
131. Huang-Mu, L.; Devanesan, S.; Farhat, K.; Kim, W.; Sivarasan, G. Improving the efficiency of metal ions doped Fe_2O_3 nanoparticles: Photocatalyst for removal of organic dye from aqueous media. *Chemosphere* **2023**, *337*, 139229. [CrossRef]
132. Li, N.; Jiang, Y.; He, Y.; Gao, L.; Yi, Z.Z.; Zhai, F.; Chattopadhyay, K. Sustainable synthesis of multiple-metal-doped Fe_2O_3 nanoparticles with enhanced photocatalytic performance from Fe-bearing dust. *J. Mater. Res. Technol.* **2021**, *15*, 810–820. [CrossRef]
133. Suresh, R.; Giribabu, K.; Manigandan, R.; Mangalaraja, R.V.; Solorza, J.Y.; Stephen, A.; Narayanan, V. Synthesis of Co^{2+}-doped Fe_2O_3 photocatalyst for degradation of pararosaniline dye. *Solid State Sci.* **2017**, *68*, 39–46. [CrossRef]
134. Yadav, P.; Dhariwal, N.; Kumari, M.; Kumar, V.; Thakur, O.P. Enhanced degradation of Congo-red dye by Cr^{3+} doped α-Fe_2O_3 nano-particles under sunlight and industrial wastewater treatment. *Chemosphere* **2023**, *343*, 140208. [CrossRef]
135. Ramprasath, R.; Arul Pragasan, L.; Manikandan, V.; Sudha, S.; Cholan, S.; Alarfaj, A.A.; Hirad, A.H.; Gokul, B.; Sampath, S. Visible light photocatalytic and magnetic properties of V doped α-Fe_2O_3 (VFO) nanoparticles synthesized by polyol assisted hydrothermal method. *Chemosphere* **2022**, *307*, 135575. [CrossRef]
136. Huang, W.; Lu, X.; Jia, D.; Huang, J.; Li, Z.; Xie, H.; Wang, M.; Li, Y.; Zhang, D. Characterization of structural, optical and photocatalytic properties of yttrium modified hematite (α-Fe_2O_3) nanocatalyst. *Ceram. Int.* **2023**, *49*, 25602–25611. [CrossRef]
137. Bhattacharya, L.; Cohen, A.; Caspary Toroker, M. Theoretical understanding of graphene supported hematite photoanode for solar-driven water splitting applications. *Catal. Today* **2024**, *442*, 114912. [CrossRef]
138. Zia, J.; Riaz, U. Microwave-assisted degradation of paracetamol drug using polythiophene-sensitized Ag–Ag_2O heterogeneous photocatalyst derived from plant extract. *ACS Omega* **2020**, *5*, 16386–16394. [CrossRef]
139. Jiang, W.; Fu, H.; Zhu, Y.; Yue, H.; Yuan, S.; Liang, B. Floatable superhydrophobic Ag_2O photocatalyst without a modifier and its controllable wettability by particle size adjustment. *Nanoscale* **2018**, *10*, 13661–13672. [CrossRef] [PubMed]
140. Naing, H.H.; Wang, K.; Tun, P.P.; Zhang, G. Enhanced broad spectrum (vis-NIR) responsive photocatalytic performance of Ag_2O/rectorite nanoarchitectures. *Appl. Surf. Sci.* **2019**, *491*, 216–224. [CrossRef]
141. Kayed, K. The luminescence properties of individual silver nanoparticles in Ag/Ag_2O composites synthesized by oxygen plasma treatment of silver thin films. *J. Lumin.* **2021**, *237*, 118163. [CrossRef]

142. Kong, Y.; Li, Y.; Cui, X.; Su, L.; Ma, D.; Lai, T.; Yao, L.; Xiao, X.; Wang, Y. SnO_2 nanostructured materials used as gas sensors for the detection of hazardous and flammable gases: A review. *Nano Mater. Sci.* **2022**, *4*, 339–350. [CrossRef]
143. Šuligoj, A.; Pavlović, J.; Arčon, I.; Rajić, N.; Novak Tušar, N. SnO_2-containing clinoptilolite as a composite photocatalyst for dyes removal from wastewater under solar light. *Catalysts* **2020**, *10*, 253. [CrossRef]
144. Mahanta, R.; Chetri, P.; Bora, D. Investigation of visible light photocatalysis effect of SnO_2 nanoparticles. *Mater. Today Proc.* **2023**, *in press*. [CrossRef]
145. Roy, H.; Ur Rahman, T.; Riad Khan, M.A.J.; Al-Mamun, M.R.; Islam, S.Z.; Khaleque, M.A.; Hossain, M.I.; Hossain Khan, M.Z.; Islam, M.S.; Marwani, H.M.; et al. Toxic dye removal, remediation, and mechanism with doped SnO_2-based nanocomposite photocatalysts: A critical review. *J. Water Process. Eng.* **2023**, *54*, 104069. [CrossRef]
146. Huong, V.H.; Nguyen, V.C.; Pham, K.P.; Nguyen, T.B.; Ngac, A.B.; Loan, T.T. Construction dual active sites on SnO_2 via Fe doping for effective ciprofloxacin photodegradation. *J. Alloy. Compd.* **2024**, *1005*, 176020. [CrossRef]
147. Shabna, S.; Sahaya Jude Dhas, S.; Biju, C.S. Potential progress in SnO_2 nanostructures for enhancing photocatalytic degradation of organic pollutants. *Catal. Commun.* **2023**, *177*, 106642. [CrossRef]
148. Hou, L.r.; Yuan, C.Z.; Peng, Z. Synthesis and photocatalytic property of SnO_2/TiO_2 nanotubes composites. *J. Hazard. Mater.* **2007**, *139*, 310–315. [CrossRef]
149. Kango, S.; Kalia, S.; Celli, A.; Njuguna, J.; Habibi, Y.; Kumar, R. Surface modification of inorganic nanoparticles for development of organic–inorganic nanocomposites—A review. *Prog. Polym. Sci.* **2013**, *38*, 1232–1261. [CrossRef]
150. Gu, X.; Lin, S.; Qi, K.; Yan, Y.; Li, R.; Popkov, V.; Almjasheva, O. Application of tungsten oxide and its composites in photocatalysis. *Sep. Purif. Technol.* **2024**, *345*, 127299. [CrossRef]
151. Zhao, Z.G.; Liu, Z.F.; Miyauchi, M. Nature-inspired construction, characterization, and photocatalytic properties of single-crystalline tungsten oxide octahedra. *Chem. Commun.* **2010**, *46*, 3321–3323. [CrossRef]
152. Chandrasekaran, S.; Zhang, P.; Peng, F.; Bowen, C.; Huo, J.; Deng, L. Tailoring the geometric and electronic structure of tungsten oxide with manganese or vanadium doping toward highly efficient electrochemical and photoelectrochemical water splitting. *J. Matter. Chem. A* **2019**, *7*, 6161–6172. [CrossRef]
153. Jiang, Z.; Liu, X.; Zhang, X.; Cui, M.; Shi, M. Efficient cleavage of C-C bond in lignin adopting Z-scheme heterojunction photocatalyst by g-C_3N_4/CQDs/WO_3. *J. Environ. Chem. Eng.* **2024**, *12*, 113898. [CrossRef]
154. Lu, J.; Wang, Y.; Liu, F.; Zhang, L.; Chai, S. Fabrication of a direct Z-scheme type WO_3/Ag_3PO_4 composite photocatalyst with enhanced visible-light photocatalytic performances. *Appl. Surf. Sci.* **2017**, *393*, 180–190. [CrossRef]
155. Ke, J.; Zhou, H.; Liu, J.; Zhang, Z.; Duan, X.; Wang, S. Enhanced light-driven water splitting by fast electron transfer in 2D/2D reduced graphene oxide/tungsten trioxide heterojunction with preferential facets. *J. Colloid Interf. Sci.* **2019**, *555*, 413–422. [CrossRef]
156. Alam, R.; Hossain, M.A.; Elias, M. Amine functionalized graphene oxide decorated with ZnO-WO_3 nanocomposites for remediation of organic dye from wastewater. *J. Phys. Chem. Solids* **2024**, *190*, 112015. [CrossRef]
157. Irani, M.; Mohammadi, T.; Mohebbi, S. Photocatalytic degradation of methylene blue with ZnO nanoparticles; a joint experimental and theoretical study. *J. Mex. Chem. Soc.* **2016**, *60*, 218–225. [CrossRef]
158. Morales, G.V.; Sham, E.L.; Cornejo, R.; Farfan Torres, M.E. Photocatalytic degradation of 2-chlorophenol by TiO_2: Kinetic studies. *Lat. Am. Appl. Res.* **2013**, *43*, 325–328.
159. Basha, S.; Barr, C.; Keane, D.; Nolan, K.; Morrissey, A.; Oelgemöller, M.; Tobin, J.M. On the adsorption/photodegradation of amoxicillin in aqueous solutions by an integrated photocatalytic adsorbent (IPCA): Experimental studies and kinetics analysis. *Photochem. Photobiol. Sci.* **2011**, *10*, 1014–1022. [CrossRef]
160. Tran, H.D.; Nguyen, D.Q.; Do, P.T.; Tran, U.N.P. Kinetics of photocatalytic degradation of organic compounds: A mini-review and new approach. *RSC Adv.* **2023**, *13*, 16915–16925. [CrossRef]
161. Liu, B.; Zhao, X.; Terashima, C.; Fujishima, A.; Nakata, K. Thermodynamic and kinetic analysis of heterogeneous photocatalysis for semiconductor systems. *Phys. Chem. Chem. Phys.* **2014**, *16*, 8751–8760. [CrossRef]
162. Gharbani, P.; Mehrizad, A.; Mosavi, S.A. Optimization, kinetics and thermodynamics studies for photocatalytic degradation of methylene blue using cadmium selenide nanoparticles. *Npj Clean Water* **2022**, *5*, 34. [CrossRef]
163. Kanwal, A.; Shahzadi, T.; Riaz, T.; Zaib, M.; Khan, S.; Habila, M.A.; Sillanpaa, M. Photocatalytic degradation studies of organic dyes over novel Cu/Ni loaded reduced graphene oxide hybrid nanocomposite: Adsorption, kinetics and thermodynamic studies. *Molecules* **2023**, *28*, 6474. [CrossRef]
164. Fatima, S.; Iqbal, M.; Bhatti, H.N.; Alwadai, N.; Huwayz, M.A.; Nazir, A.; Igbal, M. Kinetics and thermodynamics studies of nickel manganite nanoparticle as photocatalyst and fuel additive. *Heliyon* **2022**, *10*, e33861. [CrossRef]